Influence of Topography and Winds on the Distribution of Water Masses on the Antarctic Continental Shelf

CHRISTOPHER Y. S. BULL,[a] DAVID R. MUNDAY,[b] AND ADRIAN JENKINS[a]

[a] *Department of Geography and Environmental Sciences, Northumbria University, Newcastle upon Tyne, United Kingdom*
[b] *British Antarctic Survey, Cambridge, United Kingdom*

ABSTRACT: Central to improving our knowledge of ocean temperature change on Antarctica's continental shelf is a better understanding of how ocean circulation drives the onshore flux of warm deep waters across the shelf break. This study uses a primitive equation ocean model to explore how the circulation regimes (throughflow and gyre—determined by basin geometry) and changes in surface stress influence the temperature structure on Antarctica's shelf seas. Given the described shelf temperature changes are largely driven by ocean circulation changes, understanding these becomes our focus. A simple barotropic model is used to describe the linear theory of the difference between the circulation regimes and their expected responses to changes in forcing. This theory informs our understanding of the barotropic circulation response of the primitive equation model. A momentum and heat budget confirm, over simulated equilibrated time scales, that when the surface forcing changes, the response is first-order linear. Consistent with previous findings, we find that climate change projection-like wind shifts (stronger westerlies that shift south) directly influence Ekman processes across the shelf break and upwell warmer waters onto the shelf. We also find that the circulation regimes influence the mean shelf temperature and the susceptibility of existing shelf temperatures to surface stress change. In a throughflow regime, there can be a complete transition in on-shelf temperatures when the transition between westerly and easterly winds shifts southward. However, we find relatively modest warming at the coast in a gyre regime. Combinations of these regimes also experience coastal warming under a constant positive offset in winds.

SIGNIFICANCE STATEMENT: The Antarctic Slope Front determines how much warm water flows onto Antarctica's continental shelf and the subsequent heat that is available to melt the ice shelves. This study explores the impact of basin geometry and wind shifts on the large-scale ocean circulation around the shelf with a focus on understanding changes in shelf temperature near an imagined ice front. Here, meridional topographic barriers change geometry, shedding insight into how different water temperatures on the shelf coalesce despite having the same initial conditions and wind forcing. Wind perturbation simulations suggest why some regions are more sensitive to shifts in winds than others. These findings highlight an underappreciated yet fundamentally important topographical constraint under future changes in winds.

KEYWORDS: Ice shelves; Southern Ocean; Channel flows; Ekman pumping/transport; Ocean circulation; Gyres

1. Introduction

The Southern Ocean (Fig. 1a) circulation has combinations of both throughflow and gyre regimes. Wind and sea ice stress determine the momentum input driving the ocean circulation in these regimes (Fig. 1b). Throughflow regime currents are the eastward-flowing Antarctic Circumpolar Current (ACC) and a shelf-confined westward flow that is effectively a combination of the Antarctic Slope Current (ASC) and the Antarctic Coastal Current. The ACC is predominantly driven by wind and buoyancy forcing and is the world's strongest current (Olbers et al. 2012); modern estimates of Drake Passage transport vary between 137 ± 7 Sv (1 Sv ≡ 10^6 m^3 s^−1) (thermal wind only; Meredith et al. 2011) and 173.3 ± 10.7 Sv for total transport (Donohue et al. 2016). Several studies in realistic settings (e.g., Masich et al. 2015) have confirmed that topographic form stress is the dominant sink of momentum in throughflow regions. Note that the ASC is not quite a circumpolar feature; it is not found along the western Antarctic Peninsula where the ACC flows along the continental slope (Thompson et al. 2018; Whitworth et al. 1998). In between the ACC and ASC is the Antarctic Slope Front (ASF), a landward thickening of the layer of cold surface waters that, through its position on the continental shelf break, regulates onshore heat transport associated with an inflow of warmer subsurface waters (Peña-Molino et al. 2016; Thompson et al. 2018). Gyre regimes form where f/h gradients are sufficiently steep to block throughflow (Nadeau and Ferrari 2015; Olbers et al. 2007; Patmore et al. 2019; Wilson et al. 2022) and are characterized by the clockwise-flowing Weddell, Ross, and Australian–Antarctic Gyres. The Weddell and Ross Gyres with transports of 30–100 and 23 ± 8 Sv, respectively, are
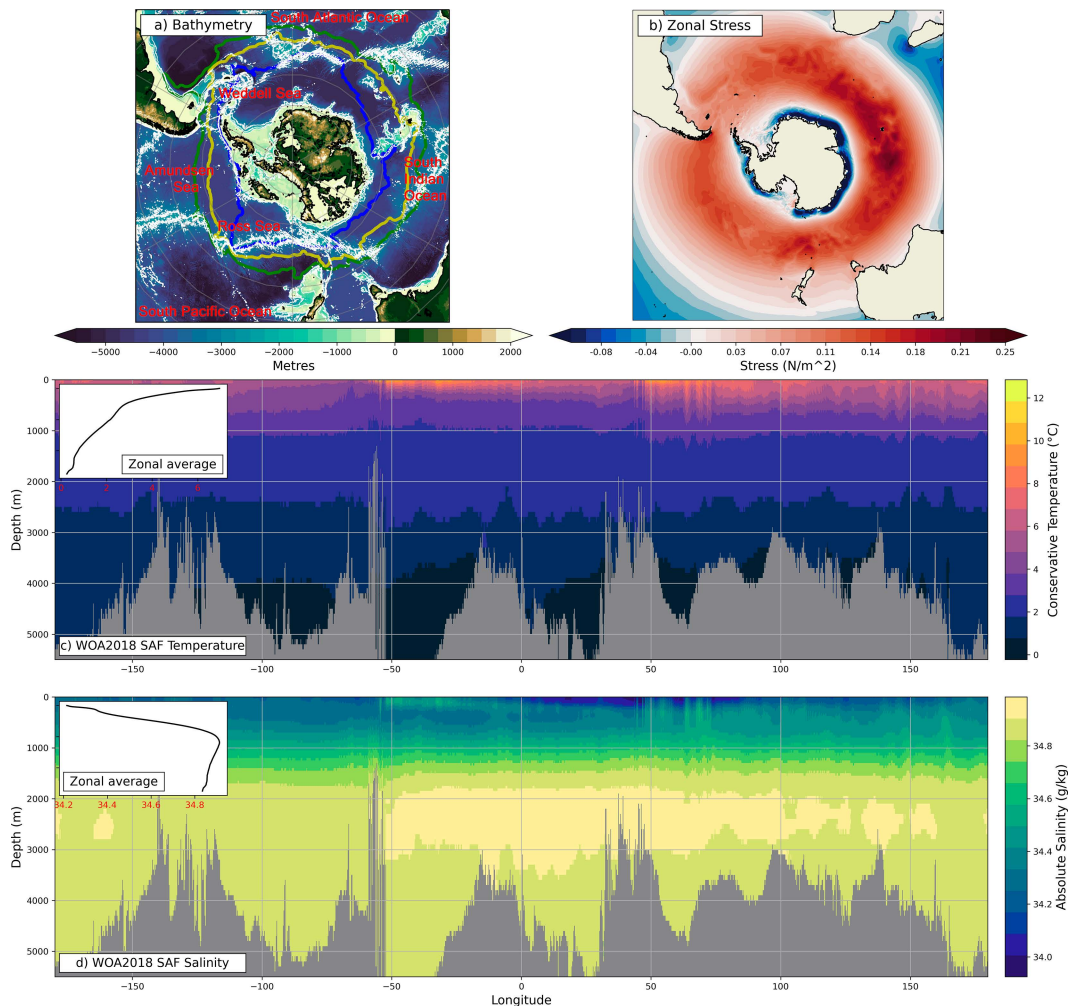
FIG. 1. (a) ETOPO1 bathymetry: Thick contours indicate southern boundary (blue), Polar Front (yellow), and Sub-antarctic Front (green) from Park et al. (2019); thin white contours highlight −3000-, −2000-, and −1000-m isobaths; and black contour is 0 m. (b) JRA zonal surface stress (time mean 1986–2000; both wind and sea ice); black contour is the surface land mask. WOA2018 Subantarctic Front [green contour in (a)]: (c) temperature and (d) salinity. The insets in (c) and (d) show the zonal average of temperature and salinity, respectively; these *T*/*S* profiles are used as initial and northern boundary restoring conditions for the modeling configuration in this study (see section 3b).

sensitive to local changes in wind stress curl (Armitage et al. 2018; Dotto et al. 2018; Gómez-Valdivia et al. 2023; Neme et al. 2021) and buoyancy forcing (Gray and Riser 2014; Hogg and Gayen 2020; Petty et al. 2013).

At the Antarctic coast, ice shelves flow from the ice sheet and are vulnerable to future changes in subsurface ocean temperatures at the southern margins. In the case of the Weddell and Ross gyres, the related ice shelves experience low area-averaged melt rates because warm water has limited direct access to the ice shelf base (Pritchard et al. 2012). Much of the recent interest in the ASF (Thompson et al. 2018) is due to its capacity to modulate the inshore flux of Circumpolar Deep Water melting the ice shelves. The ASC is driven by the along-slope westward wind stress (Pauthenet et al. 2021; Thompson et al. 2018) and buoyancy forcing (Hattermann 2018). The winds over the Southern Ocean vary on several time scales,

and all of the Southern Ocean current systems are expected to show some sensitivity to the projected southward shift in winds (e.g., Bracegirdle et al. 2013; Goyal et al. 2021), although a signal has not necessarily been observed (e.g., Armitage et al. 2018; Stewart 2021).

Considerable work has gone into understanding the antici-pated changes in Southern Ocean circulation as a result of changes in the westerly winds, particularly the circumpolar transport of the ACC (e.g., Farneti et al. 2015; Munday et al. 2013; Purich and England 2021; Spence et al. 2017). Eddy sat-uration is a regime in which the ACC's total transport be-comes insensitive to surface wind stress changes. Substantial work has gone into characterizing the eddy saturation of the ACC and relating it to eddy processes (Gnanadesikan and Hallberg 2000; Straub 1993; Tansley and Marshall 2001). In an eddy-saturated state, despite the total transport not

changing, we would expect the barotropic transport to respond to changes in surface forcing (Constantinou and Hogg 2019). Using a more realistic configuration, Spence et al. (2014) have shown that anticipated southward shifts in the Southern Ocean winds lead to a change in Ekman dynamics at the coast. Follow-up studies have looked at spatially limited anomalies (Spence et al. 2017; Webb et al. 2019) and changes in the easterly winds (Morrison et al. 2023), but these studies have not separated the influence of changes in wind intensity and wind stress curl. Spence et al. (2014) describe a mechanism as follows: Reduced Ekman pumping at the coast leads to a flattening of isotherms, enabling increased inflow of warm waters onto the shelf. Presently, there is a tendency to apply these arguments around all of Antarctica (Spence et al. 2014; Verfaillie et al. 2022). However, some regions are more susceptible to these shifts than others. Under a uniform 4° southward shift, the Amundsen Sea warms the most, whereas the Ross Sea cools and the Weddell Sea shelf modestly warms (Fig. S5b in Spence et al. 2014). Meridionally uniform changes to the winds would not be expected to change the horizontal circulation of a gyre regime but would have a strong response in a throughflow regime (Olbers 1998; Vallis 2017; Veronis 1996). The work to date has focused on southward wind shifts (stronger westerlies) that assume a throughflow-like regime. This suggests that we might be overestimating the effect of these wind shifts on Southern Ocean circulation. A natural question arises: Given the projected wind changes are similar to a positive constant offset in the winds (westerly strengthening and southward shift), how do we expect the Southern Ocean to respond in places where there are a mixture of throughflow and gyre regimes? To begin work on this last question, we review the seminal linear theory of throughflow and gyre regimes.

In their canonical form, a circumpolar-like throughflow (e.g., Antarctic Circumpolar Current) and an ocean gyre (e.g., Weddell Gyre) can be created in an open reentrant channel with a uniform wind and a closed box with a half-cosine wind, respectively (Vallis 2017). In the reentrant channel case (hereafter, "throughflow regime"), a uniform eastward wind drives an eastward current. Eddy saturation aside, increasing the strength of the wind uniformly might be expected to drive a stronger eastward current. The closed box (hereafter, "gyre regime") analog might feel like a paradox in comparison; adding a uniform wind to the half-cosine wind does not strengthen the circulation (Hughes 1997). This is because the circulation strength depends on the wind stress curl. Here, the curl is the meridional gradient of zonal velocity, and thus, a uniform change in wind does not change the horizontal circulation (Veronis 1996). In a throughflow regime, e.g., a reentrant channel with a flat bottom, a momentum budget reveals a primary balance between zonal momentum inputs from the wind balanced by bottom friction. The flat bottom results in an unrealistically strong ACC and a large sea surface height (SSH) gradient (Hidaka and Tsuchiya 1953; Munday et al. 2015; Olbers et al. 2007). Munk and Palmén (1951) showed that in the presence of significant bathymetry (hundreds of meters high), topographic form stress (as it is now known) is a more effective sink of momentum, slowing down the eastward

flow and creating a meridional geostrophic flow that is confined to below the height of the bathymetry. In contrast, in a gyre regime, the insightful perspective (Hughes 1997; Olbers 1998; Styles et al. 2022) is taken via the curl of the momentum equation. For this system, a vorticity budget reveals a primary balance between the curl of the wind stress acting as a source of vorticity and the curl of the bottom friction (flat bottomed) or the curl of the topographic form stress (significant bathymetry) acting as a vorticity sink. This profound importance of boundary conditions has led to the tendency to focus on these distinct dynamical balances when studying throughflows as compared to gyres (Olbers et al. 2012; Vallis 2017). As the real system exhibits both kinds of flows, we need a better understanding of the transitory dynamics of these two regimes so we can better predict how they will change as their forcing evolves with climate change.

The goal of this study, then, is to revisit throughflow and gyre regimes in the context of an idealized Southern Ocean configuration with southward (uniform offset) wind shift experiments. The community, for the purpose of attribution, needs to understand the implications of a change in wind strength, shifts, and curl change; using uniform offsets makes progress toward disentangling these issues. We will use barotropic linear theory to better understand the differing response to a uniform change in surface stress in a throughflow versus a gyre regime. We then investigate, with a primitive equation ocean model, how the system is complicated by the inclusion of a continental shelf, combinations of flow regimes, and baroclinicity. While the integrated changes in horizontal circulation from a reentrant channel to a hard wall are well known (e.g., Olbers 1998; Tansley and Marshall 2001; Vallis 2017), we believe this is the first time an incremental mixture of these two regimes has been studied in terms of wind shifts and the temperature structure on the shelf. Two questions arise:

1) Subject to the same starting point, how are the mean shelf temperatures influenced by a hierarchy of basin geometries?
2) How is basin geometry important for modulating shelf temperature changes with shifts in the winds?

The paper is presented as follows. Section 2 has a synthesis of existing linear theory as related to throughflow and gyre regimes in the Southern Ocean where changes in forcing are also considered. The remainder of the paper builds on this understanding using the primitive equation model Nucleus for European Modelling of the Ocean (NEMO) and adding complexity through a continental shelf, deep-ocean ridge, and walls that create combinations of throughflow and gyre regimes. The numerical model description, experiment design, and results are discussed in sections 3a, 3b, and 4, respectively. A summary and discussion are given in section 5.

2. Southern Ocean circulation theory: Throughflow versus gyre regimes

Figure 2 utilizes the Stommel (1948) planetary geostrophic equations to highlight throughflow and gyre circulations
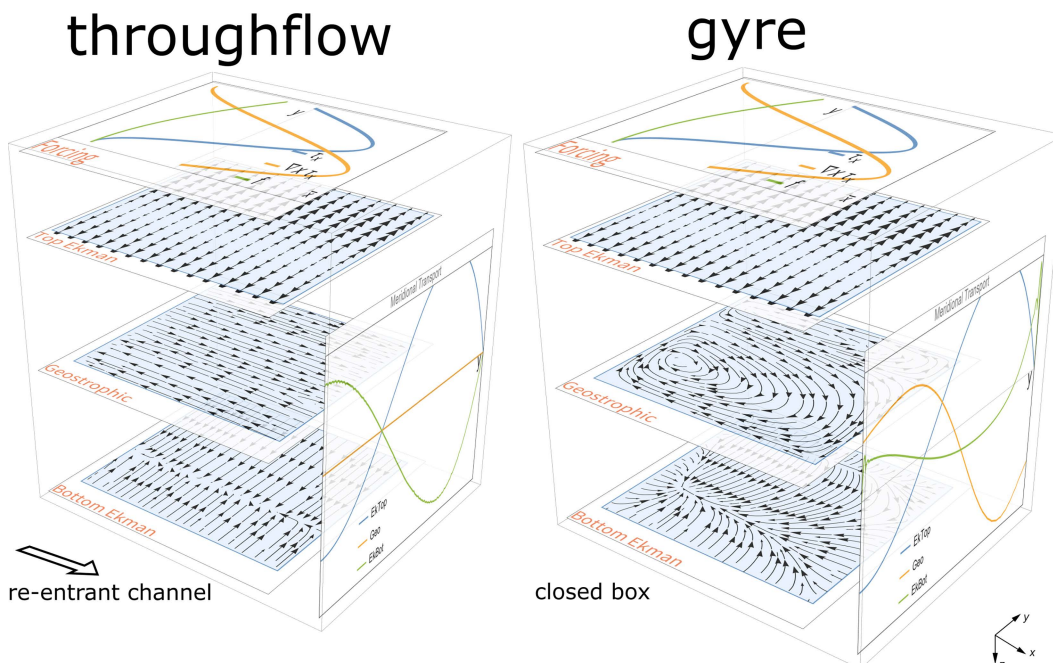
FIG. 2. Comparison of (left) throughflow and (right) gyre regimes for an idealized Southern Ocean wind stress in a single-layer ocean. The channel case has a reentrant east–west boundary, whereas the gyre case has walls on all sides. Horizontal layers show the forcing, Ekman, and geostrophic layers. The "forcing" layer shows the zonally averaged wind stress, wind stress curl, and Coriolis parameter. The circulation layers are as follows: (top) Ekman transport; (middle) geostrophic transport; and (bottom) Ekman transport. The barotropic streamfunction is the sum of these three layers (see Fig. 3). The vertical panel shows the zonally averaged meridional transport for each component.

within an idealized, barotropic, flat-bottom configuration and rigid lid. The idea of using this simple model is that it offers a heuristic setting for our theoretical barotropic expectations for what may happen in a more complex primitive equation ocean model with baroclinicity and a shelf (section 4). Having said this, to emphasize the relevance to the reader, this section does highlight some of the complex model results from section 4 as appropriate. Our 2D, nondimensionalized equations are

$$f\mathbf{k} \times \mathbf{u} = -\nabla p - r\mathbf{u} + \boldsymbol{\tau}_x,$$

$$\nabla \cdot \mathbf{u} = 0,$$

where f is the Coriolis parameter—negative for the Southern Ocean, $\mathbf{u}$ is a two-dimensional velocity vector, p is the pressure, r is a friction coefficient, $\boldsymbol{\tau}_x$ is a zonal stress, and ∇ operates horizontally. The nondimensionalization process is described in the appendix. A zonal surface stress (Fig. 2), inspired by the observed pattern (Fig. 1), is used. Hereafter, "surface stress" and "wind stress" will be used interchangeably. Compared to previous Southern Ocean idealized studies (e.g., Abernathey et al. 2011), the wind stress here includes easterlies and has a nonzero stress in the south where we imagine an ice shelf front. A change in the boundary condition, from a reentrant east–west channel to a wall, leads to fundamental changes in the circulation (section 2a). We discuss throughflow and gyre regimes in terms of the pictured

layers in Fig. 2: top (τ_x/f) and bottom ($-r\mathbf{u}/f$) Ekman and geostrophic ($-\nabla p/f$) transports. The full transport (the sum of the three layers) is shown in Fig. 3. Note that, here, all three layers are really taking place in one slab of fluid and the transports in the pictured layers are diagnostic. Circulation in the top Ekman layer is common to both regimes, but the means by which the lower layers balance the momentum input are different due to the change in boundary condition (section 2a). Practically, for Figs. 2 and 3, variables u, v, and p are solved with a finite-element method in Mathematica, and then, the Ekman and geostrophic transports are found diagnostically using the above relations. In section 2b, we use these equations to study the changes in a throughflow and gyre regime under a constant offset in winds. In section 4, we will return to these ideas but with a primitive equation ocean model with discrete z^* levels which solves a depth-dependent momentum equation. The simple approach used here highlights the linear dynamics relevant to our wind shift experiments in section 4 and shows how prescribed wind stress sets up the circulation in the lower layers.

a. Commonalities and differences to both throughflow and gyre regimes

As pictured in Fig. 2, in both throughflow and gyre regimes, the top (near surface) Ekman transport is the same. In the Southern Hemisphere, the top Ekman transport is directed 90° to the left of the surface stress and surface Ekman suction
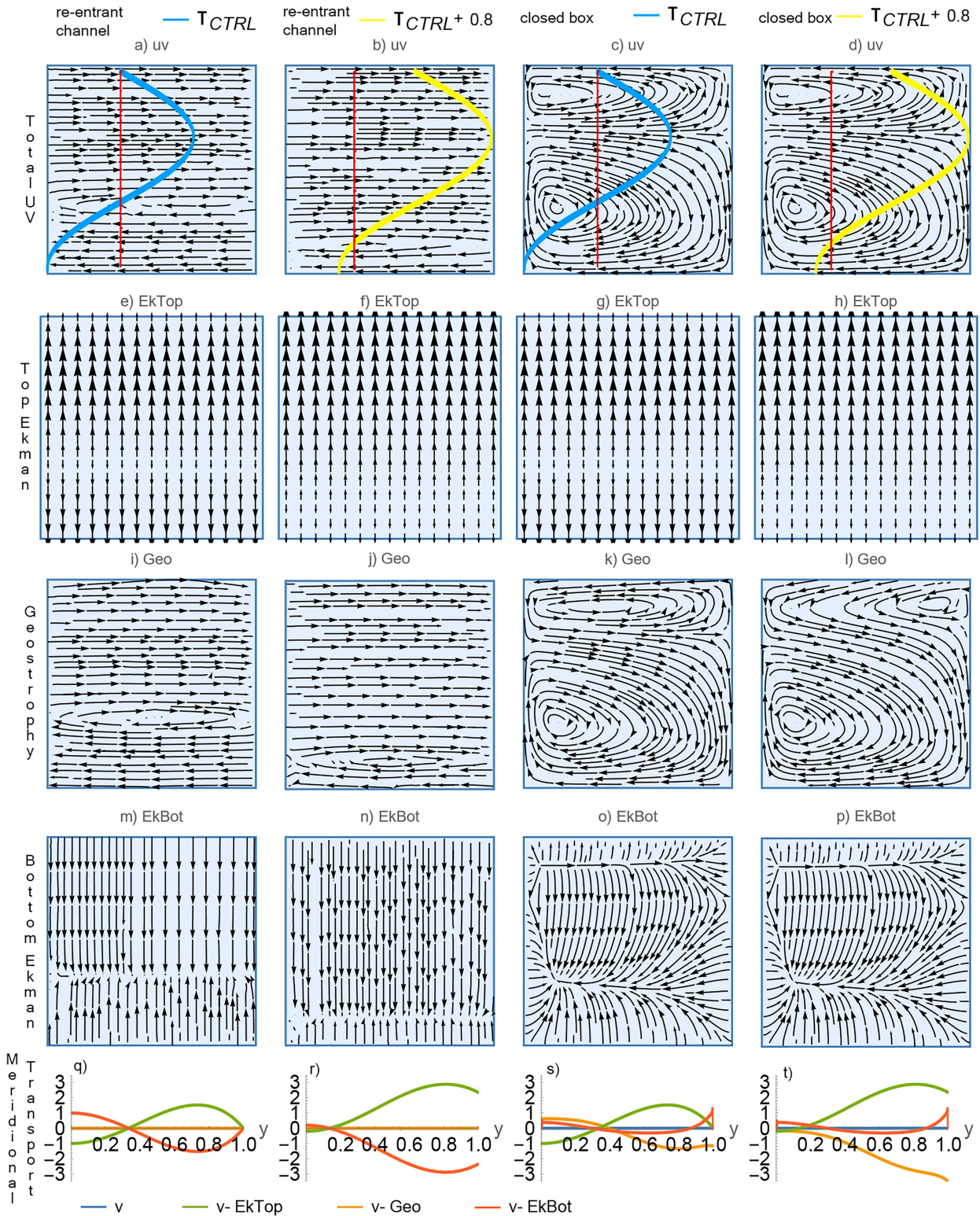
FIG. 3. Using the Stommel planetary geostrophic equations to study the changes in a throughflow and gyre regime under a constant offset in winds. Comparison of throughflow (in the first and second columns) and gyre (in the third and fourth columns) regimes for a single-layer ocean with a CTRL (τ_{CTRL}) and perturbed ($\tau_{\mathrm{CTRL+0.8}}$) idealized Southern Ocean wind stress; the overlay in the first row shows the wind forcing. Like Fig. 2, the channel case has a reentrant east–west boundary, whereas the gyre case has walls on all sides. (first row) Barotropic circulation; (second row) Ekman transport; (third row) geostrophic transport; (fourth row) Ekman transport; and (fifth row) mean meridional transport.

and pumping arises due to divergences and convergences, respectively, in the top Ekman transport (e.g., Karnauskas 2020). Here, a change from cyclonic to anticyclonic wind stress curls leads to a change from upwelling to downwelling regions on either side of the maximum westerlies. We thus expect upwelling south of the peak westerlies and downwelling to the north. Approaching the boundaries for the "control" wind stress shown, the curl goes to zero in the south but is nonzero in the north; hence, only the northern boundary will have curl-driven downwelling. We have no normal flow conditions at the southern and northern boundaries, so at the southern wall the nonzero easterly wind by continuity leads to downwelling. In contrast, the northern wall goes to zero stress, and so the wind at the boundary does not drive "continuity driven" downwelling. We will return to these ideas when considering wind shifts.

In a throughflow regime, the top Ekman transport leads to a meridional pressure gradient that drives geostrophic currents that match the wind direction (Fig. 2, throughflow, geostrophic layer); this is enabled by the reentrant boundary. The bottom Ekman transport then flows to the right of the geostrophic transport returning the flow transported by the top Ekman layer (Fig. 2, throughflow, meridional transport panel). Here, a Stommel linear friction is used, so the bottom Ekman transport is 90° to the right of the geostrophic transport (rather than 135° for the Ekman solution; Olbers et al. 2012). Top and bottom Ekman pumping and suction balance locally so there is no vertical stretching or squeezing of fluid columns, and the flows are purely zonal. Thus, in a zonally averaged throughflow regime, we have clockwise and anticlockwise overturning cells where the latitude of zero wind stress delineates the boundary between the two cells that are driven by the westerly and easterly winds, respectively.

In a gyre regime, the no-normal flow condition of the eastern and western boundaries results in dramatic changes. In the geostrophic layer, the depth-integrated circulation consists of a balance between the meridional advection of planetary vorticity and the wind stress curl (i.e., Sverdrup balance); in the return flow boundary layer, the advection of planetary vorticity is balanced by the curl of bottom friction (e.g., Waldman and Giordani 2023). As in the throughflow case, the top Ekman transport is prescribed, and this sets off an identical top Ekman pumping and suction pattern where the resulting circulation is now constrained by walls on all sides. Since the geostrophic flow is largely horizontally nondivergent, Ekman pumping/suction through the top and bottom Ekman layers results in stretching and squeezing of fluid columns in the geostrophic layer (McWilliams 2011; Pedlosky 1996). The sum of the Ekman and geostrophic components gives the depth-integrated transport. Unlike a throughflow regime, a gyre regime has geostrophic zonal and meridional flows that are nonuniform in x. Also, unlike in a throughflow regime, the meridional return transport is no longer confined to the bottom Ekman layer but also to the geostrophic return flow (Fig. 2, gyre, meridional transport panel). This is because in a throughflow regime, there is no western wall to support a pressure gradient, and so there can be no geostrophic meridional transport.

b. Linear responses of both systems to wind shifts

In this section, we apply a constant positive, zonally uniform change in wind stress of 0.8 to the system considered in section 2a (Fig. 2); control (CTRL) and CTRL + 0.8 are shown in Fig. 3. As the perturbation is a constant offset of the wind profile (top row overlay in Fig. 3), the wind stress curl does not change. In an idealized sense, this is similar to what we expect with climate change: an increase in the strength of the westerly winds, a weakening of the easterlies, and a shift of the easterly–westerly transition zone south. Changes in the top Ekman layer are common to both regimes (Figs. 3e–h), but the means in which the lower layers balance the momentum input are different due to the different boundary conditions. In a throughflow regime, as 0.8 is added to the wind stress (column 2 in Fig. 3), the north–south sea surface height gradient associated with the zonal geostrophic flow gets stronger, and so it directly modifies the strength of the zonal geostrophic currents (see also section 4c and Fig. 10). In a gyre regime, however, the zonal Sverdrup transport is related to the gradient in the wind stress curl, and thus, the zonal transport is locked. In both regimes, the curl is not changing so neither can the region nor magnitude of upwelling and downwelling. The magnitude of Ekman transport does change, so, by continuity, the downwelling transport at the northern and southern boundaries has to change, and in this instance, an increase in one leads to a compensating decrease in the other.

In a throughflow regime, the eastward and westward jets associated with the eastward and westward stresses increase and decrease in strength, respectively. When 0.8 is added to the wind stress, the geostrophic eastward jet accelerates leading to the bottom Ekman transport commensurately increasing (Fig. 3r). Most importantly, the two Ekman overturning cells described earlier in this section shift south (Figs. 3e,f,m,n,q,r). Since the latitude of the easterly–westerly transition zone has shifted south, the upwelling of the northern cell has also shifted south; this change will be a crucial feature in our numerical experiments in section 4. So, how is it that a change in surface stress can have such a dramatic effect in a throughflow regime as compared to a gyre?

Veronis (1996) and Vallis (2017) provide some clues for how we can understand the gyre regime response. Consider the case of a uniform, zonal, eastward wind applied to the gyre case. That would set up a northward top Ekman transport which would drive an eastward geostrophic current. The eastward geostrophic current would create a raised sea surface height in the east, driving a geostrophic current southward.[1] Bottom Ekman transport aside, this geostrophic current would return the volume displaced by the original northward top Ekman transport. At equilibrium, there would be no zonal flow, and hence no meridional bottom Ekman transport, but there would be a closed meridional overturning circulation with northward transport in the top Ekman layer balanced by a southward geostrophic flow set up by the west–

---

[1] In contrast, in the throughflow case, the increased zonal momentum input is balanced by stronger bottom friction.
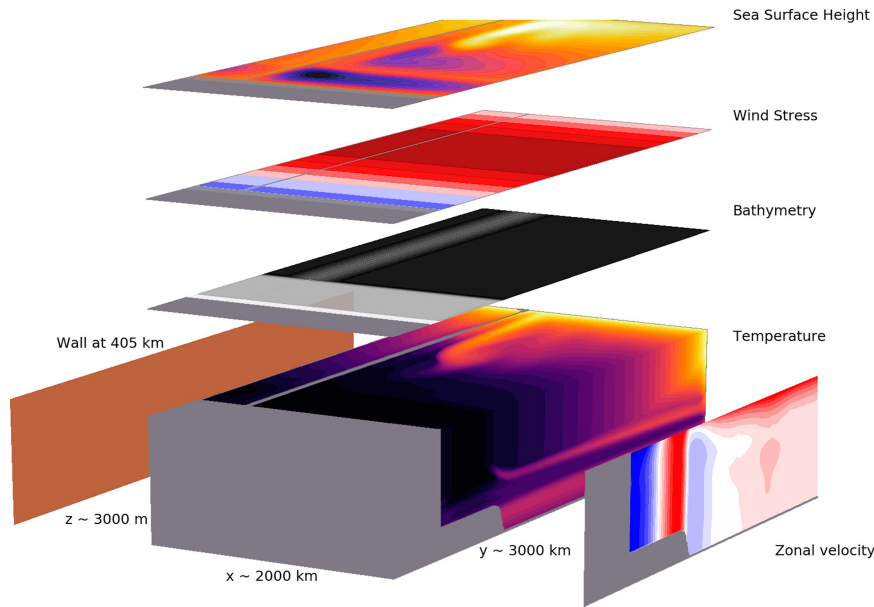
FIG. 4. A 3D snapshot of the model's temperature field from a gyre experiment. The temperatures range from −1.9° to 1.5°C. Overlaid above are SSH (from −5 to 20 cm); CTRL wind stress τ_0 (from −0.05 to 0.2); and bathymetry. (right) Zonal-mean zonal velocity (from −20 to 20 cm s^{-1}). (left) Most experiments have some kind of wall at 405 km rising from either the shelf or deep-ocean ridge; here, there is a wall, the full length of the domain. Note the vertical scale is stretched.

east gradient in sea surface height. Moreover, if we were to uniformly increase the strength of the wind, at equilibrium, we would only expect an increase in the west–east gradient of sea surface height (21.7.6 in Vallis 2017) and an associated increase in the meridional overturning. Returning to the wind stress in Fig. 3, since the total circulation streamfunction is determined by the curl of the stress and our constant offset (0.8) has no curl, it does not change the total streamfunction (Figs. 3c,d). Exploiting our simple previous example, the sea surface height gradient change only depends on the sign of offset, not on the direction of the winds. Moreover, for the total streamfunction to not change (Figs. 3c,d and 11, bottom row), the vertical structure of the flow has to compensate via a change in upwelling or downwelling at the northern and southern walls (see also Fig. 10, bottom row).

Veronis (1996) shows that a constant offset of the stress affects both the Ekman and geostrophic transports in a compensating manner (Figs. 3s,t). While very large offsets are explored in that study, we will consider smaller changes in this study. Veronis (1996) suggests that the compensation occurs equally between geostrophic and top Ekman components; however, the bottom Ekman is not considered. Since the zonal Sverdrup transport is related to the gradient in the wind stress curl and we only have zonal winds here, the geostrophic compensation will occur in the meridional transport. In Fig. 3, two right columns, as we add 0.8 to the forcing: The top Ekman transport moves uniformly up as the geostrophic transport uniformly shifts down to compensate (Stommel 1957, and Figs. 3s,t). Spatially, we see that the geostrophic transport entirely compensating for changes in the top Ekman transport is accomplished by a rearrangement of the northern gyre (Figs. 3k,l). With this kind of forcing change and model formulation, there is no change in the bottom Ekman because there is no change in curl and the bottom Ekman transport depends on $-r\mathbf{u}/f$.

TABLE 1. Key parameters used in the configuration with model reference winds τ_0.

Symbol	Value	Description
L_x, L_y	2003.7, 3025 (km)	Domain size
H	3047 (m)	Depth of domain
Δ_x, Δ_y	7.9 (km)	Horizontal resolution
Δ_z	1 (m) surface–135 (m) depth	Vertical resolution
f_0	-1.46×10^{-4} (s^{-1})	Southern boundary Coriolis
f_y	-1.28×10^{-4} (s^{-1})	Northern boundary Coriolis
L_{EW}	770 (km)	Value of y where winds transition from easterly to westerly
$L_{easterlies}$, $L_{westerlies}$	385, 2239 (km)	Distance over which the easterly and westerly winds blow
τ_E, τ_w	-0.05, 0.2 (N m^{-2})	Peak easterly and westerly wind stress
eiv	2000 m^2 (s^{-1})	GM constant eddy-induced diffusivity parameterization

The consequences of this simple barotropic linear theory will now be explored in a primitive equation ocean model (e.g., Fig. 6). Of key interest to us is how a more sophisticated numerical model (e.g., baroclinicity, nonlinear momentum, shelf break and deep-ocean ridge, and combination of flow regimes) will add complexity to the response.

3. Model and experimental design

a. NEMO model configuration

The ocean general circulation model used in this study is version 4.0.4 of the NEMO model (Madec et al. 2019). NEMO solves the incompressible, Boussinesq, hydrostatic primitive equations with a split-explicit free-surface formulation. NEMO here uses a z^*-coordinate (varying cell thickness) C grid with partial cells at the bottom-most layers to provide a more realistic representation of bathymetry (Barnier et al. 2006). Our model settings include a 55-term polynomial approximation of the reference Thermodynamic Equation of Seawater-2010 (TEOS-10: IOC et al. 2010), nonlinear bottom friction, a free-slip condition at the lateral boundaries, energy- and enstrophy-conserving momentum advection scheme, and a prognostic turbulent kinetic energy scheme for vertical mixing. Laterally, we have constant eddy coefficients with a Laplacian operator for both lateral diffusion of tracers and momentum, using eddy diffusivity coefficients of 100 and 600 $m^2\,s^{-1}$, respectively.

The modeling setup is pictured in Fig. 4 with key parameters in Table 1. The modeling domain is on a β plane with 257×385 regularly spaced points in x and y, respectively. The relatively coarse resolution of the model (7.9 km) was necessary here due to the high number of simulations (next subsection). Stewart and Thompson (2015) found that 1 km or finer is required to resolve eddies for cross-shelf heat transport. However, on the larger scale, Stewart and Thompson (2012) found that 5 km was sufficient. Here, to mitigate our lower resolution, we use the Gent–McWilliams (GM) eddy parameterization (Gent et al. 1995; Gent and Mcwilliams 1990) to represent the effects of unresolved mesoscale eddies on tracer distribution, i.e., temperature, salinity, and other tracers. We choose eiv = 2000 $m^2\,s^{-1}$ based on Allison et al. (2011) and Visbeck et al. (1997). The ocean floor is limited to 3023 m and is represented by 61 vertical levels, where the vertical grid is ~1 m at the surface and 135 m at the lowest level with initial thicknesses taken from the 75-level DRAKKAR formulation used in realistic configurations (e.g., ORCA025). Walls exist on the northern and southern boundaries in all experiments. The western–eastern boundary is fully reentrant, but in some cases, it is effectively blocked. Figure 4, for example, is effectively in a gyre regime due to a wall at 405 km. The external forcing is a restoring condition (toward the initial state) at both the northern boundary and near surface. Additionally, there is a surface wind stress (Fig. 4). The simulations are initialized from rest with initial conditions derived from World Ocean Atlas (WOA) 2018 (Boyer et al. 2018). These fields are then set as the surface restoring condition as the simulation evolves. The northern restoring condition is shown in Fig. 1 insets (7-day restoring time scale) and found by taking the WOA zonal average of profiles along the Subantarctic Front from Park et al. (2019), pictured in green in

Fig. 1a. The near-surface restoring is then found by taking the surface WOA zonal average of temperature/salinity in between the Antarctic coast and the Subantarctic Front, normalizing for NEMO's grid points. Similar to other studies in the literature (Wilson et al. 2022; Zhai and Munday 2014), here, we use a 10-m restoring thickness and 10-day restoring time scale. The configuration has no ice shelf, sea ice, or tides but is inspired by previous Southern Ocean idealized channel modeling (e.g., Abernathey et al. 2011; Morrison et al. 2011), where the interest here was to have a simple system in which to understand the momentum balance's role in setting shelf properties from wind stress forcing alone. All simulations in this paper have a spinup of 90 years where the time-mean values of a further 10 years are used for all analyses. Spinup metrics including domain-averaged SSH and domain-integrated salinity, temperature, and kinetic energy, combined with test simulations of 370 years, suggest that the 90-yr spinup is sufficient to capture the equilibrated response of the ocean circulation to the forcing.

b. Experimental design

1) SURFACE FORCING AND BATHYMETRY

Given the idealized nature of this study, we choose an idealized surface forcing and boundary conditions. The wind stress forcing is the same zonally throughout the domain (meridional wind stress is zero) and is intended to represent a zonal average of the Southern Ocean's easterlies and westerlies [Fig. 1b; JRA-55-do (Tsujino et al. 2018)]:

$$\tau_c(y) = \begin{cases} 0, & 0 < y < 393\,(\text{km}) \\ \tau_E \times \sin\!\left(\dfrac{-0.5\,\pi y}{L_{\text{easterlies}}}\right) + c, & 393 \le y \le 770\,(\text{km}) \\ \tau_W \times \sin\!\left(\dfrac{\pi y}{L_{\text{westerlies}}} - \dfrac{L_{EW}\pi}{L_{\text{westerlies}}}\right) + c, & 770 \le y \le 3025\,(\text{km}) \end{cases},$$

where $c = 0$ is the control simulation (τ_0). Four additional values of c give the four perturbation forcings: $\tau_{-0.1}$, $\tau_{-0.05}$, $\tau_{0.05}$, and $\tau_{0.1}$. The wind stress fields used are shown graphically in Fig. 5a. We briefly consider how the idealized forcings relate to present-day conditions, comparing Figs. 1a and 1b with Fig. 5a. Figures 1a and 1b show that over most of the shelf, the winds are eastward with small areas of westward winds in the western side of the Weddell and Ross Seas. The change in sign in wind direction typically occurs near the shelf break (e.g., Amundsen Sea) or offshore. Thus, the $\tau_{-0.05}$ and $\tau_{-0.1}$ forcings are most relevant to present conditions and the τ_0, $\tau_{0.05}$, and $\tau_{0.1}$ forcings are most relevant to projected (idealized) future conditions. To emulate the geometry of the Southern Ocean (see Fig. 1a and section 1 discussion), we then have four different bathymetries (Fig. 5, middle and bottom rows). All bathymetries have the same deep-ocean 900-m high meridional ridge (Figs. 5b,d,f,h), seafloor, and zonally uniform shelf (gray line in Fig. 5a). The first case (δ_{NONE}) only consists of the ridge and shelf, whereas cases 2–4 (δ_{swall}, δ_{oowall}, and δ_{wall}) have a wall at 405 km that is two grid cells wide and rises out of the top of the deep-ocean ridge. Since the western–eastern boundary is reentrant, the construction of a wall is effectively changing the boundary condition. Thus, in the case of δ_{NONE}, we are in a
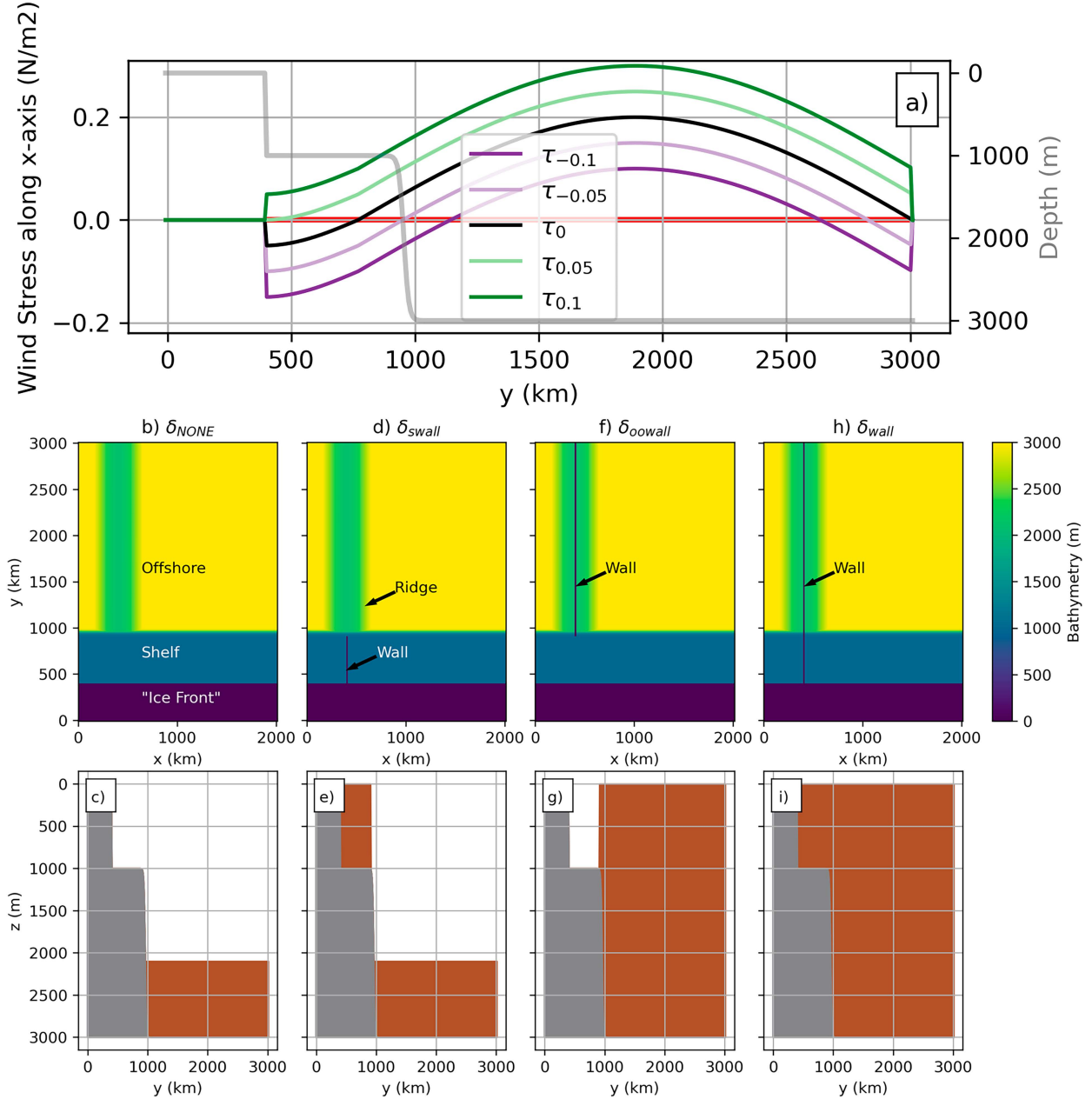
FIG. 5. (a) Five zonally uniform wind stress forcings applied to each of the four bathymetries in the bottom panels; black τ_0 is the CTRL simulation, and perturbation experiments are created by adding ($\tau_{0.05}$, $\tau_{0.1}$) or removing ($\tau_{-0.05}$, $\tau_{-0.1}$) a constant. Red horizontal line at zero highlights the transition from easterlies to westerlies, where applicable. Gray line (twin axis, scale on right) shows the shelf, common to all experiments (i.e., δ_{NONE}). The middle and bottom rows show the four different bathymetries δ_{NONE}, δ_{swall}, δ_{oowall}, and δ_{wall} used to create different "boundary conditions." (b)–(i) Prescribed bathymetry used for experiments 1–20 (surface forcing shown in Fig. 1), and each column is a new bathymetry. (middle) Plan view. (bottom) Meridional slice where gray shows the bathymetry (unchanged across all bathymetries) and brown shading in (b)–(d) shows the wall at $x = 405$ km (approximately). All experiments are listed in Table 2.

throughflow regime and in δ_{wall} gyre regime. The remaining two cases will lead to combinations of regimes; namely, δ_{swall} will have a gyre on the shelf/throughflow offshore, whereas δ_{oowall} will have a gyre offshore/throughflow on the shelf, respectively. Furthermore, when the shelf is blocked with a wall (δ_{swall}), the wall ends on the shelf permitting throughflow on

the slope, and the opposite is true when the deep ocean is blocked by a wall (δ_{oowall}).

2) EXPERIMENTS

From Fig. 5, we have five different surface forcings (Fig. 5a; $\tau_{-0.1}$, $\tau_{-0.05}$, τ_0, $\tau_{0.05}$, and $\tau_{0.1}$) and four different bathymetries
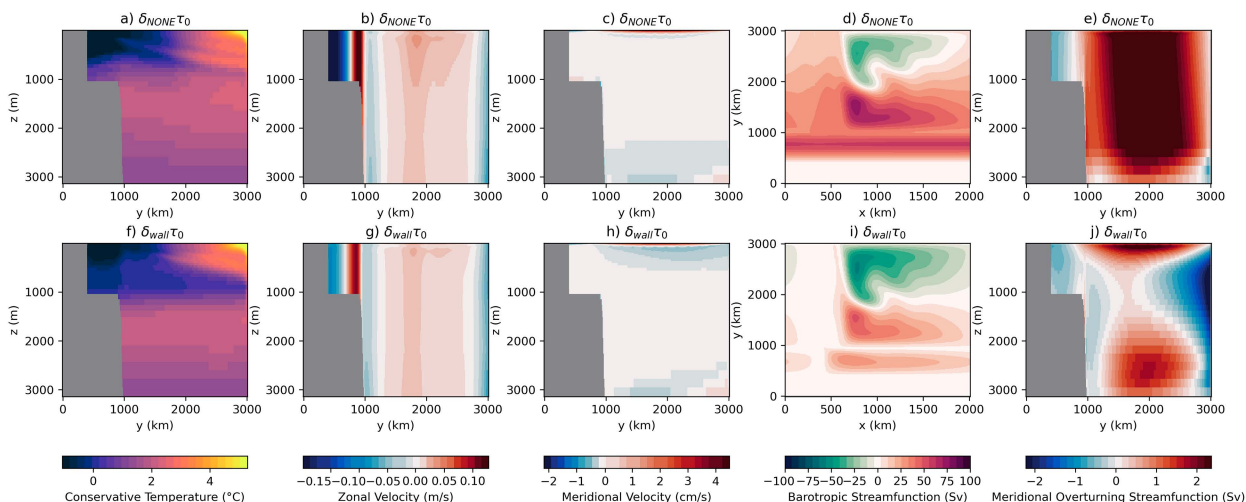
FIG. 6. Overview of (top) the mean state of the open reentrant channel δ_{NONE} and (bottom) fully closed box δ_{wall} with CTRL wind stress τ_0. (first column) Conservative Temperature (°C), (second column) zonal velocity (m s^{-1}), (third column) meridional velocity (cm s^{-1}), (fourth column) barotropic streamfunction (Sv), and (fifth column) meridional overturning streamfunction (Sv) where the first three are the zonal average.

(Fig. 5, middle and bottom rows; δ_{NONE}, δ_{swall}, δ_{oowall}, and δ_{wall}). Taking the combinations leads to 20 experiments (Table 1). The simulations are designed to highlight the dependence of the strength and location of the ASF to changes in boundary conditions and changes in surface forcings.

4. Numerical results

a. Summary of NEMO's mean state circulation for throughflow and gyre regimes

Figure 6 shows the mean circulation metrics of the two "bookend" cases with a control surface stress, namely, $\delta_{\mathrm{NONE}}\tau_0$ which is in a throughflow regime and $\delta_{\mathrm{wall}}\tau_0$ which is in a gyre regime. Comparing Figs. 6a and 6f, the throughflow case has relatively warm waters on the shelf compared to the gyre regime case. The circulation metrics in the subsequent columns are broadly consistent with the linear circulation discussed in section 2 (Fig. 2), although the addition of more complex physics and geometry does lead to some new features. Having added a ridge in the deep ocean, the barotropic streamfunction in the open channel (Fig. 6d) has partially blocked flow over the ridge and unblocked throughflow on the shelf. In contrast, the closed box (Fig. 6i) has gyres both on the shelf and in the deep ocean. In Fig. 6i, compared to section 2a, the addition of a shelf introduces steep f/h gradients, leading to an additional gyre in the south (the same direction as the curl is unchanged over that region). Figures 6d and 6i also have nonlinear, eddy features (standing eddies, meanders, and eddy recirculation) in between the gyres due to vorticity transport (Stewart et al. 2021). Comparing Figs. 6b and 6g, the zonal flows in Fig. 6g are consistent with the three gyres observed in Fig. 6i, or like Fig. 2, but with the additional gyre on the shelf. Relatedly, Figs. 6b and 6d are not like Fig. 2 as a throughflow because the zonal flows are dominated by the gyres created through the deep-ocean ridge. Sensitivity tests highlight that the zonal flow (Fig. 6b)

does look like Fig. 2 (left) in the absence of the ridge (not shown).

Looking at the meridional velocities in Figs. 6c and 6h, transport in the top and bottom layers is also consistent with section 2a. In particular, the latitude in which the transport changes direction in the top and bottom layers in a throughflow regime coincides with the change in the wind direction. As expected, in a throughflow regime, the return flow is confined to a bottom Ekman layer on the shelf and distributed over the height of the ridge (900 m) in the deep ocean (geostrophic), whereas in a gyre regime, the geostrophic return flow is higher in the water column. Considering the Eulerian overturning streamfunction, for a throughflow regime (Fig. 6e), we have clockwise and anticlockwise overturning cells that are separated by the change in wind direction. For a gyre regime (Fig. 6j), two similar cells are much closer to the surface and we have an additional three subsurface cells that arise from the change in zonal currents (Fig. 6g).

b. Shelf temperatures are modulated by winds and circulation regime

Understanding how temperature on the shelf changes (Figs. 7 and 8) as the ocean circulation changes across all the experiments in Table 2 (Figs. 9–14) is a key objective of this study. Figure 7 shows the shelf response in terms of zonally averaged temperature, and Fig. 8 highlights the heat that is available on the southern boundary to be transported beneath an imagined ice shelf (not represented here but planned as future work). Figure 7 shows that there are two mechanisms by which the strength and structure of the warm water inflows on the shelf can be altered by shifting the winds (Fig. 7, columns) or by creating a gyre via a change in the boundary constraint (Fig. 7, rows). Looking down any Fig. 7 column where the coastal downwelling is fixed, we note that the boundary
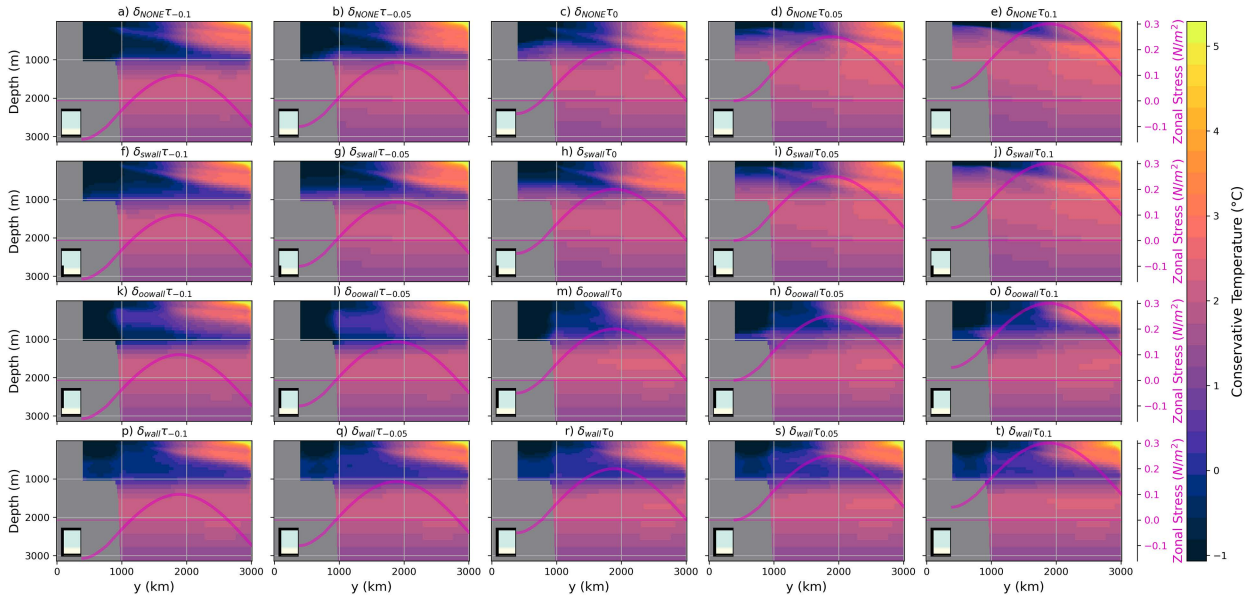
FIG. 7. Zonal-mean temperature for all experiments (Table 2). Each column has a new wind stress forcing (Fig. 5a) where the middle column is the CTRL wind stress. The magenta line highlights the zonally averaged wind stress. Each row has a different boundary condition, on the order of (i) fully reentrant, (ii) blocked shelf, (iii) blocked deep ocean, and (iv) fully blocked shelf and deep ocean. The small glyphs (at the bottom left) schematically indicate the geometry under consideration in each panel. This panel-experiment layout applies to Figs. 7–12, 14 and Figs. S1–S4, S6–S9.

constraint is a key factor in determining the intensity and location of the ASF. For example, focusing on the central column (control wind stress τ_0), the warmest waters reach the southern boundary when the shelf has a wall (Fig. 7h), whereas the presence of a deep-ocean gyre (fully blocked offshore) reduces the temperature of warm waters on the shelf (Figs. 7c,m). The blocked shelf cases (Fig. 7s, row; δ_{swall}) are warmer than

the reentrant cases (Fig. 7, first row; δ_{NONE}) since the gyre on the shelf creates a return flow that is driven by the zonal geostrophic currents (Fig. S2 in the online supplemental material). In particular, the eastward current near the shelf edge drives a southward geostrophic current which enables warm water inflows. Additionally, the winds are another key constraint. Looking left to right across the rows, a southward shift in the
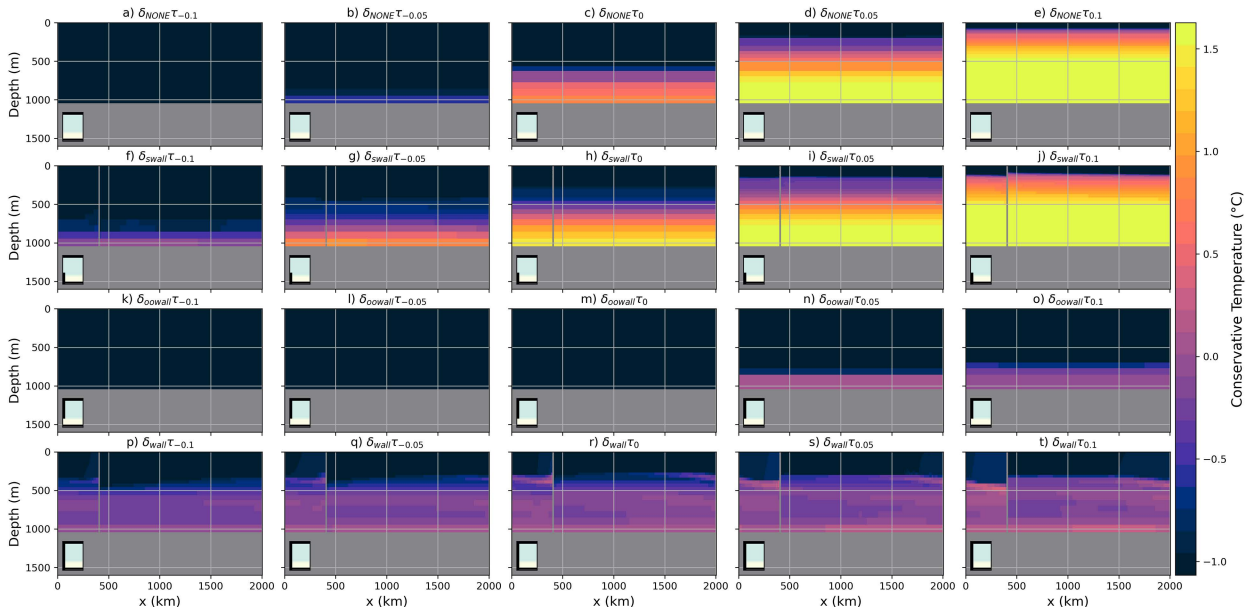

FIG. 8. The same panel-experiment layout as in Fig. 7, but for the southern boundary ("Ice Front" indicated in Fig. 5b) mean temperature.

TABLE 2. List of experiments. Name indicates the bathymetry δ and surface forcing τ_c used where $c = 0$ is the CTRL surface forcing. See Fig. 5 for details.

Number	Name	Boundary condition is				Surface forcing c
		Fully open	Shelf block	Deep-ocean block	Fully closed	
1	$\delta_{NONE}\tau_{-0.1}$	✓				-0.1
2	$\delta_{NONE}\tau_{-0.05}$	✓				-0.05
3	$\delta_{NONE}\tau_{0}$	✓				0
4	$\delta_{NONE}\tau_{0.05}$	✓				0.05
5	$\delta_{NONE}\tau_{0.1}$	✓				0.1
6	$\delta_{swall}\tau_{-0.1}$		✓			-0.1
7	$\delta_{swall}\tau_{-0.05}$		✓			-0.05
8	$\delta_{swall}\tau_{0}$		✓			0
9	$\delta_{swall}\tau_{0.05}$		✓			0.05
10	$\delta_{swall}\tau_{0.1}$		✓			0.1
11	$\delta_{oowall}\tau_{-0.1}$			✓		-0.1
12	$\delta_{oowall}\tau_{-0.05}$			✓		-0.05
13	$\delta_{oowall}\tau_{0}$			✓		0
14	$\delta_{oowall}\tau_{0.05}$			✓		0.05
15	$\delta_{oowall}\tau_{0.1}$			✓		0.1
16	$\delta_{wall}\tau_{-0.1}$				✓	-0.1
17	$\delta_{wall}\tau_{-0.05}$				✓	-0.05
18	$\delta_{wall}\tau_{0}$				✓	0
19	$\delta_{wall}\tau_{0.05}$				✓	0.05
20	$\delta_{wall}\tau_{0.1}$				✓	0.1

transition zone from westerlies to easterlies increases the intensity of warm waters on the shelf (see also Fig. S1). This shift is most effective, however, when the winds are shifted over an open channel region (Fig. 7, rows 1–3) where the northern Ekman overturning cell's upwelling region is shifted south of the shelf break. This process was outlined with linear theory in section 2b (Fig. 3), namely, in a throughflow regime,

as a positive offset is added, the upwelling associated with the northern Ekman overturning cell shifts south. In short, the presence of a wall increasingly hinders the capacity of the winds to drive warmer waters across the shelf, and so the winds are maximally effective in a fully throughflow regime (Figs. 7a–e; δ_{NONE}). The other extreme then is the introduction of a full north–south wall (Fig. 7, row 4; δ_{wall}) where changes in the
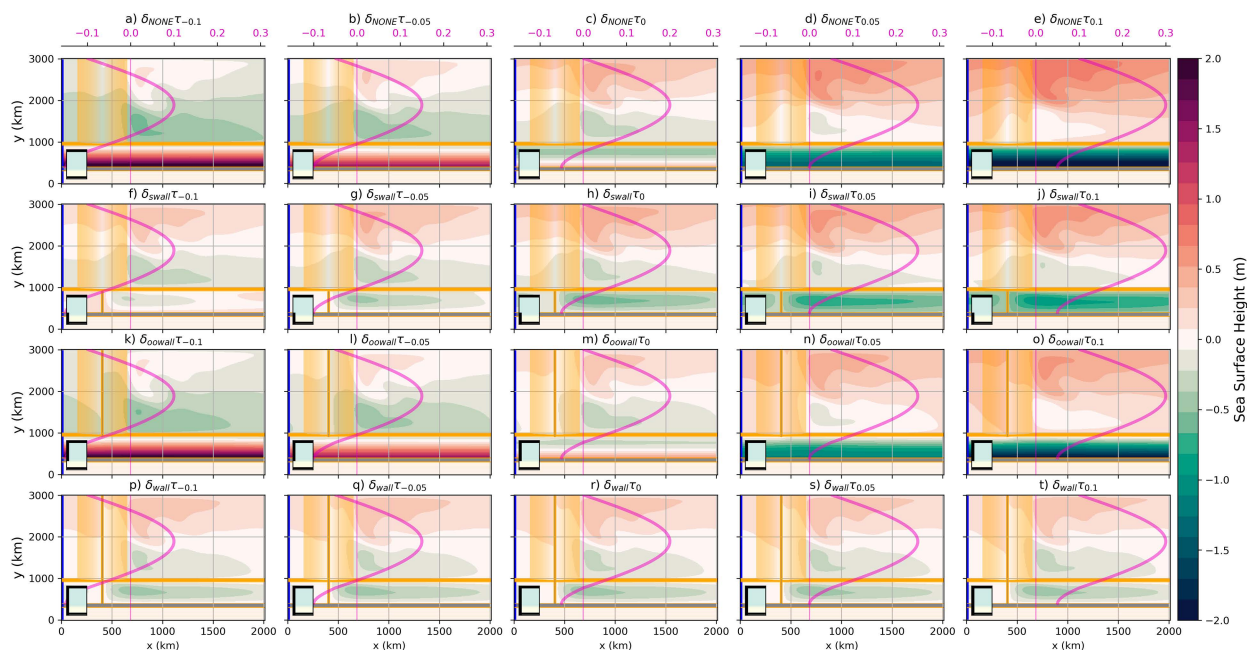

FIG. 9. The same panel-experiment layout as in Fig. 7, but for SSH for all experiments. Thin yellow lines are isobaths. The magenta line highlights the zonally averaged wind stress.
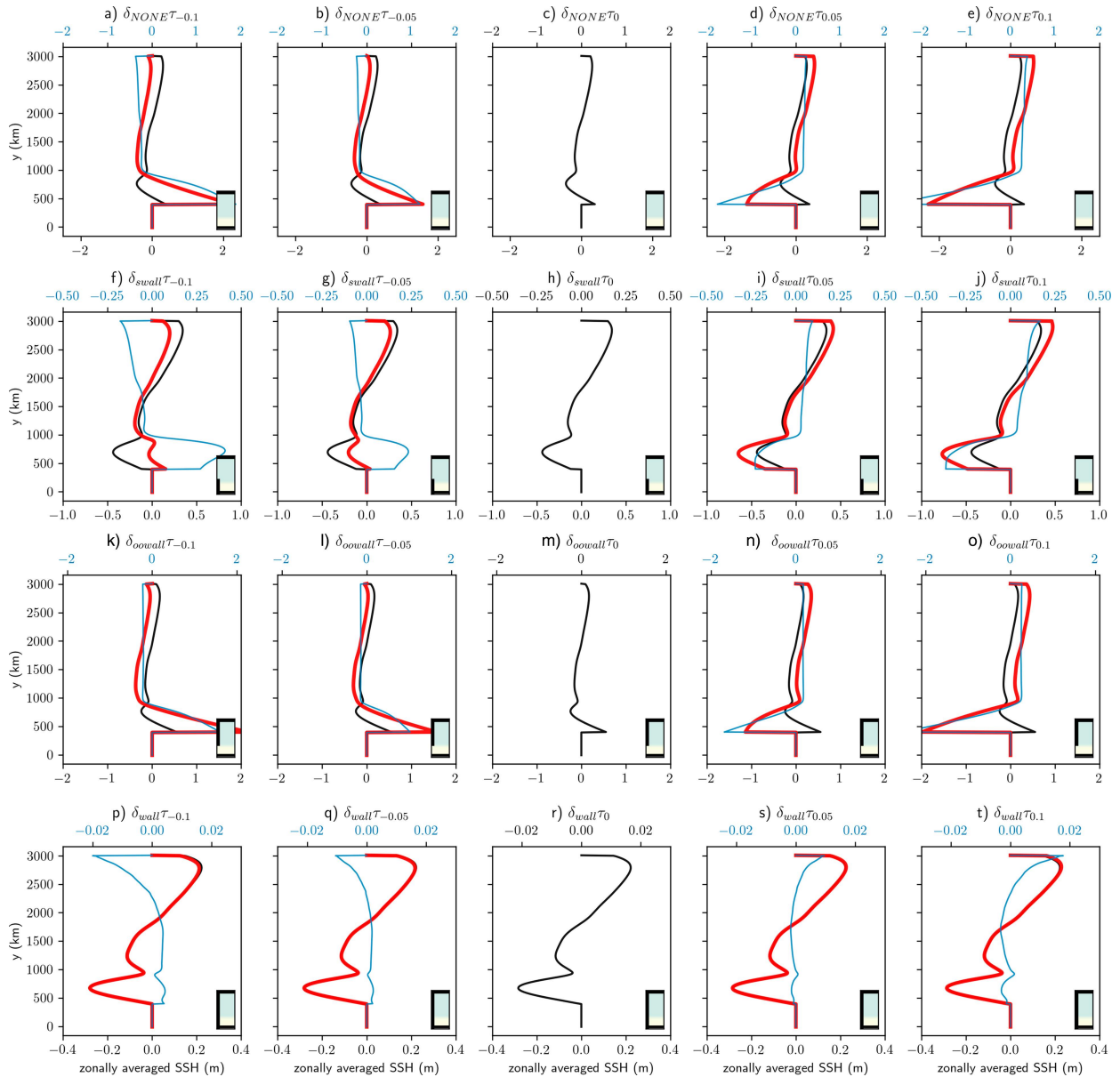
FIG. 10. Zonal-mean SSH for all experiments with the same panel-experiment layout as in Fig. 7. In all panels, black is the CTRL simulation (wind stress offset $c = 0$) where the CTRL experiment changes on each row. The red line is the perturbed stress experiment, and the blue is the difference between the two (top; alternative x axis with blue scale). If comparing rows, one should focus on the red lines in the perturbed experiments and the black line for the central column. Also, note the differing scales on the domain axis.

winds are no longer able to (dramatically) change the amount of warm waters on the shelf. This is due to there being no change in the (total) horizontal circulation in the presence of a wall because, by design, changes in τ_c do not change the wind stress curl—how this is achieved baroclinically is discussed in section 4d. Finally, a wall in the deep ocean (Fig. 7, row 3; δ_{oowall}) flattens isotherms in the deep ocean, thus reducing the amount of available heat close to the shelf break to be brought up onto the shelf when the winds are shifted.

Subsurface temperature changes at our imagined ice front are particularly relevant to ice shelves, so Fig. 8 refines our

focus toward the zonal temperature changes at the southern boundary. Due to the presence of a wall and changes in top Ekman transport, we expect and observe differences in downwelling at the southern boundary (e.g., Figs. 8f–h). Comparing rows, introducing a gyre on the shelf is important because it has warmer ice front temperatures; this is seen by comparing Figs. 8f, 8g, and 8h (gyre present) with Figs. 8a–c and 8k–m (throughflow present). In these instances, the wall on the shelf provides the most effective transport of shelf edge temperatures to the ice front by enhancing the cross-shelf transport of waters. Only in the presence of a wall is
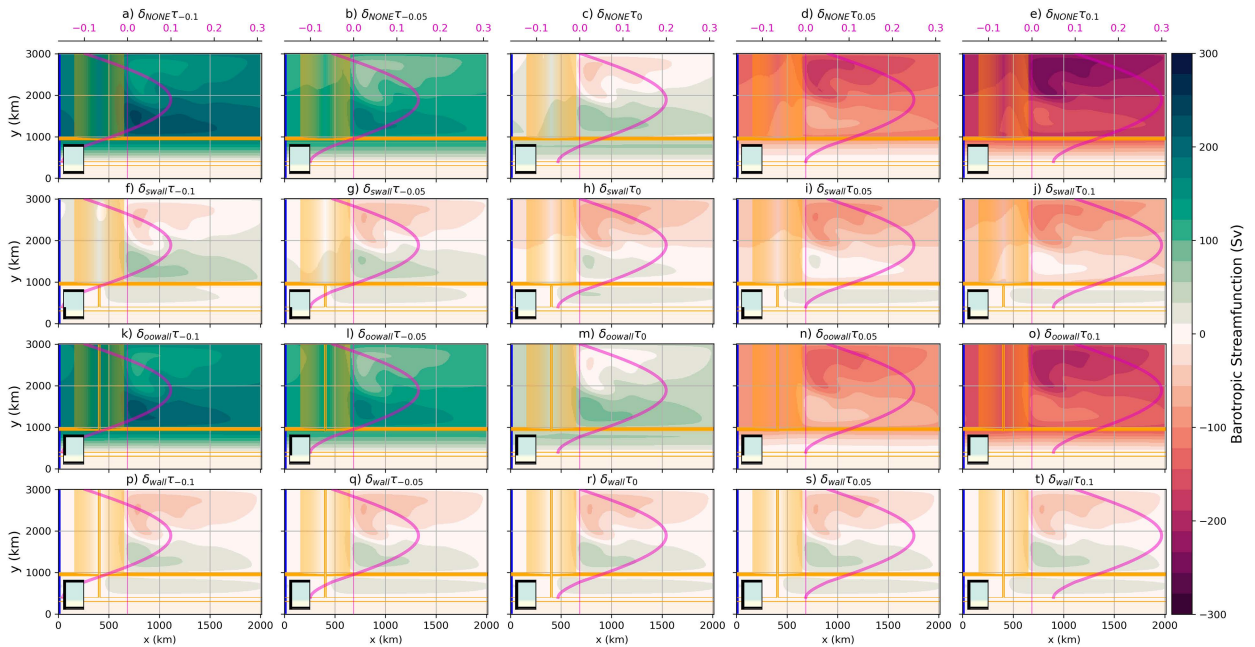
FIG. 11. The same panel-experiment layout as in Fig. 7, but now with the barotropic streamfunction for all experiments. Thin orange lines are isobaths. The barotropic streamfunction is defined here with $u_{BS} = -\partial\psi/\partial y$ and $v_{BS} = \partial\psi/\partial x$, where they are found from the vertically integrated model transport. For example in (r), the streamfunction shows an anticyclonic (counterclockwise) gyre in the north and two cyclonic (clockwise) gyres in the south.

there any meridional geostrophic flow. When the shelf is open (Fig. 8, row 1), waters cannot cross the shelf edge so effectively, so even when the winds push warm waters onto the outer shelf, they do not get to the ice front. The deep-ocean gyre's importance is readily seen by comparing the δ_{wall} simulations (Fig. 8, row 4) with the other boundary conditions (Fig. 8, rows 1–3); the δ_{wall} simulations have a

zonal structure and temperature variability with depth. The caveat is that the deep-ocean gyre is only important when both the shelf and deep ocean are blocked (comparing Fig. 8 rows 1 and 3 and rows 2–4), the system is evidently nonlinear. As compared to Fig. 7, Fig. 8 shows nuanced changes with the δ_{wall} simulations in terms of the zonal temperature structure (Fig. 8, row 4). Figure 7 row 4 suggests that δ_{wall}
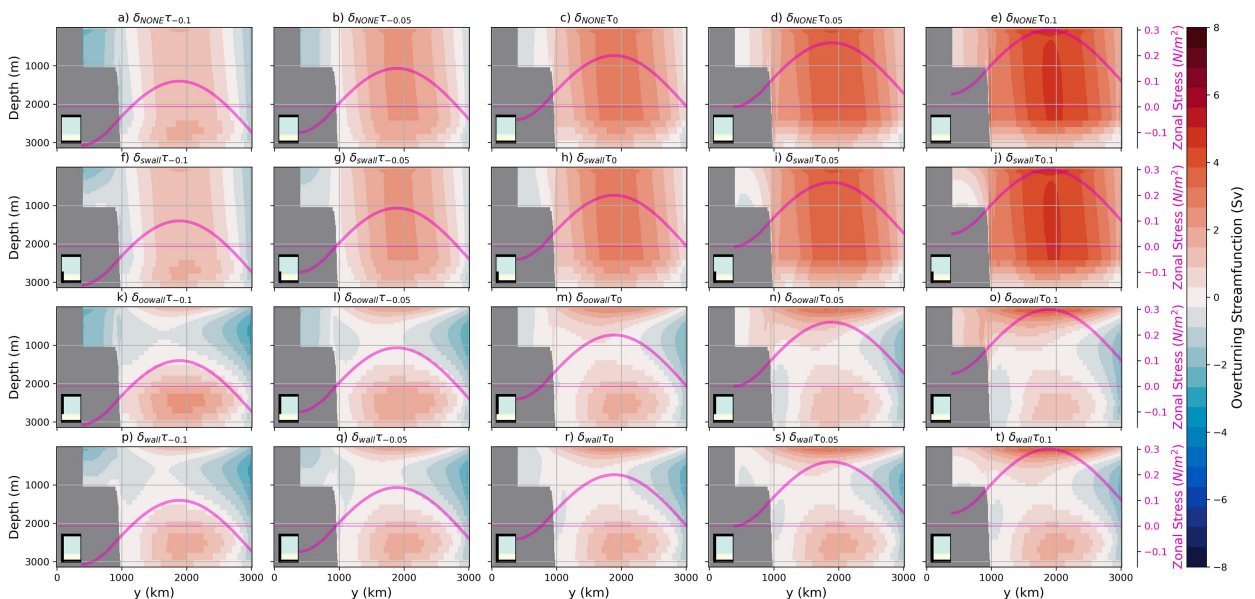

FIG. 12. The same panel-experiment layout as in Fig. 7, but now the meridional overturning streamfunction for all experiments.
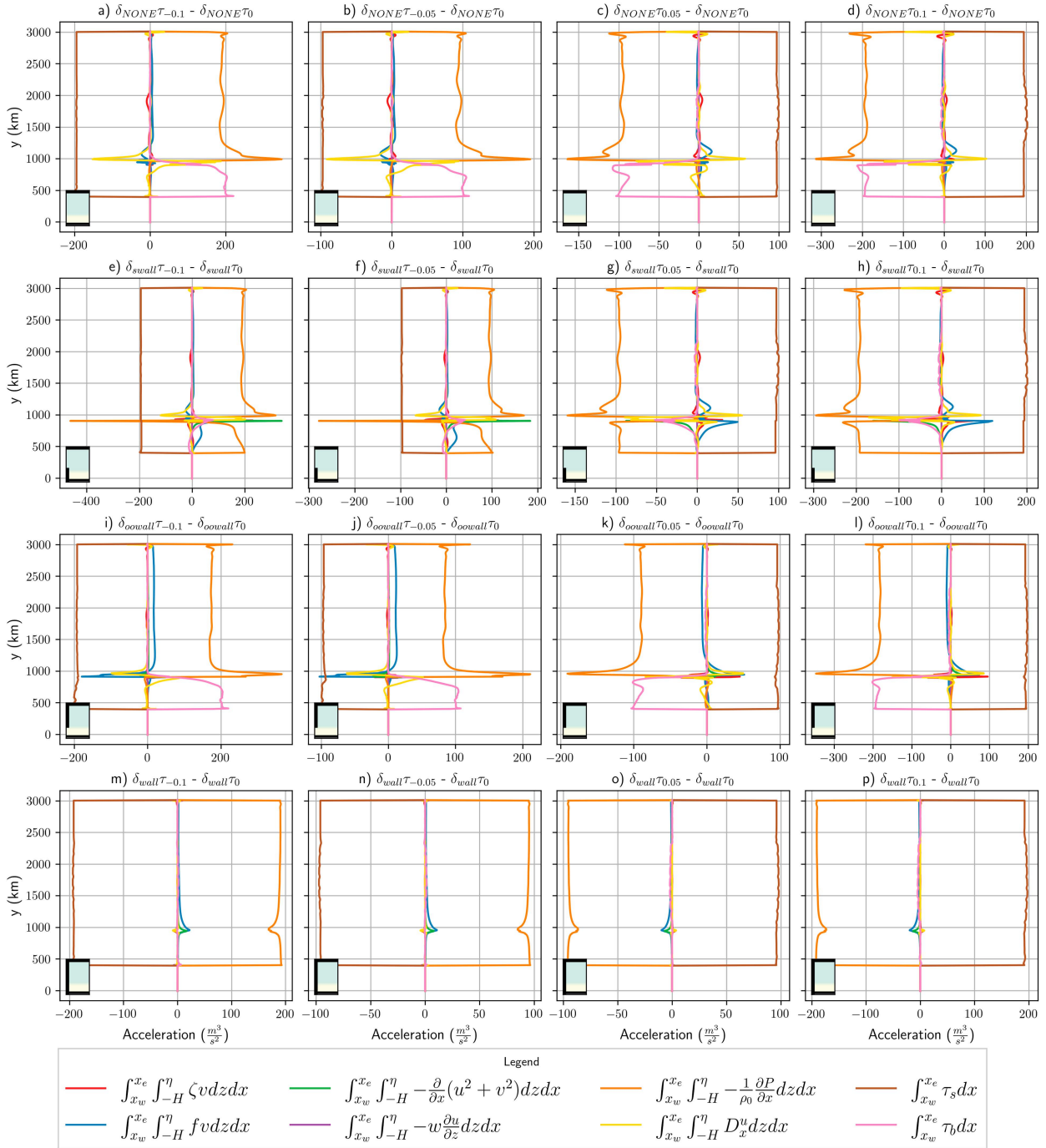
FIG. 13. The 10-yr time-average vertically and zonally integrated zonal momentum budget with anomalies from the CTRL wind experiment shown. The terms are as described in section 4e and indicated by the legend. Each row has a different boundary condition, on the order of (i) fully reentrant, (ii) blocked shelf, (iii) blocked deep ocean, and (iv) fully blocked shelf and deep ocean, respectively. The small glyphs (in the bottom left) schematically indicate the geometry under consideration in each panel.

removes almost any sensitivity to changes in wind stress (Fig. S1 shows a weak sensitivity). Figure 8, however, shows zonal changes with a small increase in temperature at the eastern boundary and along the shelf seafloor as a constant offset to the winds is added (Fig. 8, bottom row). This is likely driven by the increase in coastal downwelling and the change in southward meridional geostrophic transport highlighted in section 2b; the underlying dynamics will be revisited with new circulation metrics in sections 4c and 4e (Fig. S5).
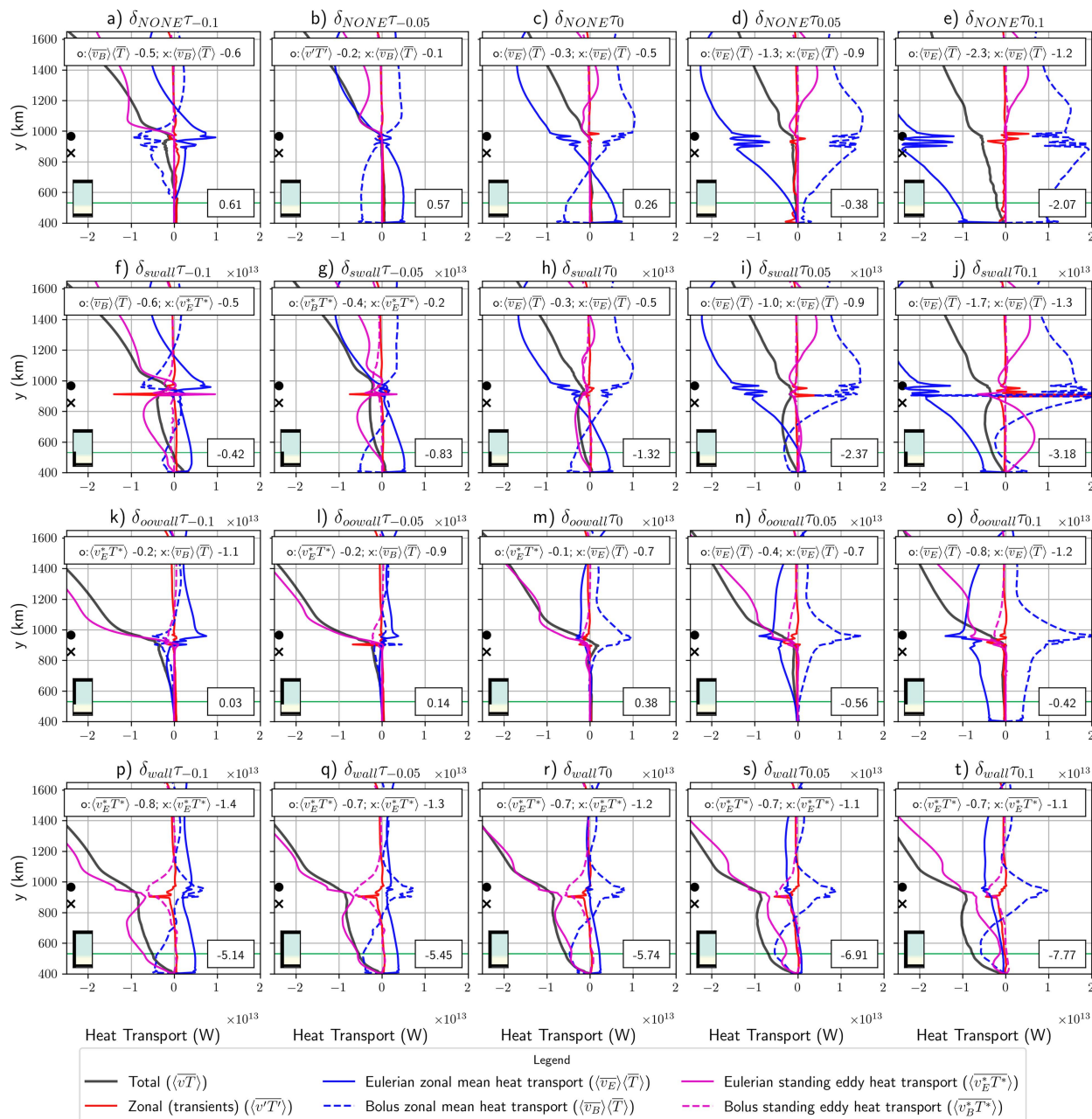
FIG. 14. The same panel-experiment layout as in Fig. 7, but now the meridional heat transport for all experiments. The terms are as described in Eq. (1) in section 4f and indicated by the legend. In each panel, the top inset gives the leading transport term and heat transport ($\times 10^{13}$) in two locations north and south of the shelf break in the open ocean (indicated by "●") and shelf edge (indicated by "x"); the total is not considered. The bottom inset in each panel gives the total heat transport across the green line ($\times 10^{12}$; black line). The small glyphs (in the bottom left) schematically indicate the geometry under consideration in each panel.

c. Understanding horizontal circulation changes due to winds and circulation regime

This section characterizes the horizontal circulation (SSH in Figs. 9 and 10 and barotropic streamfunction in Fig. 11) changes that lead to the described differences in shelf temperatures (section 4b). Similarities and differences to the linear response (section 2) are also highlighted where relevant.

Figures 9 and 10, like Figs. 3i–l, highlight how the near-surface geostrophic transport responds to changes in boundary conditions under the same top Ekman transport. Like in section 4a, we start with the two bookend cases ($\delta_{NONE}\tau_0$ and $\delta_{wall}\tau_0$). Comparing Figs. 9c and 9r, due to the deep-ocean ridge blocking the barotropic flow, the throughflow case is dominated by the influence of the gyre regime (the shelf region is the exception). In the control throughflow and gyre

cases, the north–south SSH gradient (Figs. 10c,r) is nonlinear as the stress has curvature and f is varying. We now briefly consider the "full" throughflow (δ_{NONE}) and gyre geometry (δ_{wall}) response to a change in surface forcing. A throughflow regime's response (top row in Fig. 9) is readily understood by considering the simpler case of when the stress is only eastward ($\delta_{NONE}\tau_{0.05}$ and $\delta_{NONE}\tau_{0.1}$ in Figs. 9d,e) or mostly eastward in the barotropic model (columns 1–2 in Fig. 3). In these cases, driven by northward top Ekman transport (Figs. 3e,f), we have a positive SSH offset in the deep ocean (Figs. 10d,e). Also, note in Figs. 10d and 10e, as compared to the control case, the largest SSH change occurs over the shelf due to the change from easterlies to westerlies over the shelf; this change is relatively large due to the shelf having a flat bottom. Looking across the whole top row of Fig. 9, the strength and positions of the westward and eastward currents on the shelf are modulated by the strength of the wind and the shift in location for the sign change in the winds (see also section 2b). Moving now to the δ_{wall} geometry's response to a change in surface forcing, since the wind stress curl is unchanged, the barotropic streamfunction is unchanged in the full gyre regime experiments (row 4 in Figs. 11 and 3c,d). Further, as expected from section 2b, the zonal-mean SSH at the northern boundary does raise and lower (upwelling/downwelling) as the strength of the offset is increased and decreased (Fig. 10 bottom row).

We now consider the horizontal circulation changes across all experiments. In all panels in Figs. 9–11, a key observation is that the presence of a ridge puts the deep-ocean region into a gyre regime. In the absence of a ridge (i.e., a flat bottomed ocean), the deep ocean looks like a throughflow regime from section 2. Moreover, the ideas from section 2b (Fig. 3) still apply here, but the signal is convoluted by the deep-ocean gyres. As an example, from section 2, we expect channel flows to be more affected by constant wind offsets than circulation in a box. Here, as we add a constant offset to the wind, the eastward flow is accelerated where the contours relating to the gyres are unchanged (e.g., top and bottom rows in Figs. 9 and 11). With this in mind, note that both SSH and barotropic streamfunction (Figs. 9 and 11) have the following features: (i) rows 1 and 3 are very similar and (ii) row 2 shows modest changes. We consider these two features:

(i) Rows 1 and 3 (throughflow and blocked deep ocean, respectively) in Figs. 9 and 11 are similar because the deep-ocean ridge blocks the barotropic flow. So, creating a wall on top of the ridge only has a limited impact on the large-scale circulation, namely, deflection/throughflow over the ridge on the first row as compared to interior return flow in the third row. Additionally, the geostrophic transport on the shelf matches the wind direction (Fig. 9), and consistent with section 2b, the zonally averaged SSH changes commensurately with changes in Ekman transport (Fig. 10).

(ii) Due to the shelf being blocked, the barotropic streamfunction (Fig. 11) on the shelf for row 2 (blocked shelf) is largely unchanged. However, similar to row 1, the streamfunction shows an eastward acceleration of the

deep-ocean jet, which is of similar magnitude to row 1 (the streamfunction integrates through a gyre which has both westward/eastward components, reducing the overall transport; see Fig. S2). Taking the difference between streamfunction and SSH (Fig. 9), we see that the gyre on the shelf has the same spatial pattern; it is just enhanced by the change in Ekman transport. A positive wind offset has more northward top Ekman transport (Figs. 10i,j), whereas a negative offset has relatively less northward top Ekman transport leading to a weaker dome (Figs. 10f,g).

d. Understanding overturning circulation changes due to winds and circulation regime

The Eulerian meridional overturning streamfunctions shown in Fig. 12 highlight how each boundary condition alters the means by which the vertical structure compensates for the changes in top Ekman transport as the stress changes. At the large scale, the overturning is throughflow dominant with boundary conditions δ_{NONE} and δ_{swall} (rows 1–2 in Fig. 12) and gyre dominant for δ_{oowall} and δ_{wall} (rows 3–4 in Fig. 12). Across all regimes, the change in the direction of the top Ekman transport coincides with the latitude at which the winds change direction (e.g., Figs. 12c,h,m,r). In a fully throughflow regime (top row in Fig. 12), the clockwise northern overturning cell (Figs. 12a–e) has its geostrophic return flow confined to the height of the ridge. Both the northern and southern (Figs. 12a–c) overturning cells are modulated by the position and strength of the westerlies/easterlies and the transition zone of the westerlies to easterlies (Figs. 12a–c). This highlights how the change in upwelling up the shelf break occurs and is consistent with the linear dynamics discussed in section 2b. It also explains the discussed shelf temperature changes (section 4b; Fig. 6). Introducing a wall on the shelf (row 2 in Fig. 12), the overturning is similar to δ_{NONE} (row 1 in Fig. 12), except that the return flow on the shelf is no longer confined to the bottom Ekman layer. Instead, it is higher up in the water column as a geostrophic return flow making the anticlockwise cell on the shelf more baroclinic. Despite there being no westward wind in Figs. 12i and 12j, there is a weak subsurface anticlockwise overturning cell on the shelf; this is likely a closure for the now opposing zonal flows (comparing Figs. S2d,e,i,j) and the geostrophic return flow created by the gyre on the shelf. The deep-ocean wall simulations δ_{oowall} (row 3 in Fig. 12) are readily understood by considering the δ_{wall} case and the above arguments. Introducing a full north–south wall (Fig. 12r) leads to three gyres and their associated overturning (see section 4a). As the winds are modified, e.g., with the uniform westward wind (Figs. 12p,q), the anticlockwise cells above 1000 m get larger and stronger. This is due to the increase in southward top Ekman transport at the southern boundary and the now southward top Ekman transport at the northern boundary. Similarly, with a uniform addition of eastward wind (Figs. 12s,t), the near-surface clockwise-overturning cell gets larger and stronger. Revisiting Fig. 6, but now with the control simulations removed (middle $c = 0$ column), Fig. S1 shows that the zonally averaged temperature does change in a consistent, modest way with these overturning

changes. The observed linking of the bottom and top overturning cells in Figs. 12s and 12t likely also explains the modest temperature changes seen in δ_{oowall} row 4 in Fig. 8. Having said this, section 4f considers the eddy advection term and revisits this link in more detail. In sections 4a–d, we have considered large-scale time-mean circulation changes. In the remaining result subsections, we examine the possible importance of eddy terms in the momentum (section 4e) and meridional advective heat (section 4f) balances.

e. Momentum budget

Several studies have found that eddies are a critical feature for fluxing heat and mass across the shelf break (Stern et al. 2015; Stewart and Thompson 2015; St-Laurent et al. 2013). Throughout this study, we have assumed that the changes in shelf temperatures are largely a result of momentum advection from circulation changes. Here, using depth-integrated and zonally integrated momentum budgets, we look to test whether these circulation changes are indeed linear (not related to eddies) and whether the described geostrophic and Ekman dynamics (sections 2 and 4c) are what is driving those changes. The NEMO vector invariant form of the momentum equation is

$$\frac{\partial \mathbf{u}_h}{\partial t} = -\left[(\nabla \times \mathbf{u}) \times \mathbf{u} + \frac{1}{2}\nabla \mathbf{u}^2\right]_h - f(\mathbf{k} \times \mathbf{u})_h - \frac{1}{\rho_0}\nabla_h P + D^u + F^u,$$

where f is the Coriolis parameter, $\mathbf{u}_h$ is the horizontal velocity vector, and ∇ and ∇_h are the 3D and 2D gradient operators, respectively. The $[\cdot]_h$ is the horizontal component of a vector. The F^u is the vertical divergence of the vertical diffusive momentum fluxes, i.e., $\partial/\partial z[\kappa_z(\partial \mathbf{u}_h/\partial z)]$, which includes the top and bottom stresses where $\int_{-H}^{\eta} F^u dz = \tau_s - \tau_b$. The D^u is the horizontal divergence of the horizontal diffusive momentum flux {i.e., $\nabla \cdot [\kappa_h(\partial \mathbf{u}_h/\partial x) + \kappa_h(\partial \mathbf{u}_h/\partial y)]$}, with the turbulent horizontal κ_h and vertical κ_Z viscosities.

Figure 13 shows the depth-integrated and zonally integrated x-momentum balance (Figs. S3 and S4 show the raw values of both x and y budgets). Compared to Figs. 7–12, Fig. 13 has four columns instead of five because we show momentum budget anomalies relative to the experiment with the control wind stress. As they are anomalies from the associated control experiment, Fig. 13 (Fig. S5) is primarily intended to be compared along the rows. Under a change in wind forcing, over a long time mean ($\partial \mathbf{u}_h/\partial t = 0$), Fig. 13 highlights the importance of bottom friction and pressure gradients in balancing the input of momentum by the wind stress. In other words, unsurprisingly, the following terms dominate:

$$\int_{x_w}^{x_e} \tau_s dx = \underbrace{\int_{x_w}^{x_e} \tau_b \, dx}_{\text{throughflow}} + \underbrace{\int_{x_w}^{x_e}\int_{-H}^{\eta} \frac{\partial p}{\partial x} dz dx}_{\text{gyre}}.$$

In regions where there are a throughflow regime and flat bottom (rows 1 and 3), the change in surface stress $\int_{x_w}^{x_e} \tau_s dx$ (light brown) is matched by a commensurate and opposite change in bottom stress $\int_{x_w}^{x_e} \tau_b \, dx$ (dark gray). In contrast, in

regions where there is a gyre regime, consistent with previous studies (Munday et al. 2015; Olbers et al. 2007), the change in surface stress $\int_{x_w}^{x_e} \tau_s dx$ (light brown) is matched by a commensurate and opposite change in the depth-integrated and zonally integrated pressure gradient $\int_{x_w}^{x_e}\int_{-H}^{\eta}(\partial p/\partial x)dz dx$ (i.e., continental/topographic form stress). As the barotropic flow is blocked in the deep ocean, this balance between wind stress and topographic form stress exists in the deep ocean across all the rows. When the shelf and entire domain are blocked (rows 2 and 4), it additionally occurs on the shelf.

Figure S5 shows the depth-integrated and zonally integrated y-momentum balance, which highlights the importance of geostrophy. As expected, with changes in winds, we see minor changes in geostrophic balance in a fully blocked gyre regime (see discussion in Fig. S5 and sections 2b and 4c).

f. Meridional advective heat transport

In section 4e, we found that nonlinear terms in the momentum budget were relatively unimportant (within the same geometries). That budget, however, does not demonstrate that eddy advection is also negligible in the temperature equation. With this curiosity in mind, Fig. 14 shows the following meridional advective heat balance:

$$\begin{aligned}
\rho_0 c_p L_x \int_{-H}^{\eta} \langle \overline{vT} \, dz \rangle &= \rho_0 c_p L_x \int_{-H}^{\eta} \langle \overline{v_E} \rangle \langle \overline{T} \rangle \, dz \\
&+ \rho_0 c_p L_x \int_{-H}^{\eta} \langle \overline{v_B} \rangle \langle \overline{T} \rangle \, dz + \rho_0 c_p L_x \int_{-H}^{\eta} \langle \overline{v_E^* \, T^*} \rangle \, dz \\
&+ \rho_0 c_p L_x \int_{-H}^{\eta} \langle \overline{v_B^* \, T^*} \rangle \, dz + \rho_0 c_p L_x \int_{-H}^{\eta} \langle \overline{v'T'} \rangle \, dz.
\end{aligned} \tag{1}$$

This balance is calculated using time averages of the product of the meridional velocity v, the temperature T, and the vertical grid spacing at v points $e3v$ at every time step, ensuring temperature advection is properly accounted for (Munday et al. 2021). Here, as we are using GM to represent the subgrid-scale mixing of tracers, we have $v = v_E + v_B$ which are the full, Eulerian, and bolus velocities, respectively (the bolus velocity is what is due to GM). The remaining variables in the above equation are as follows: The $\rho_0 = 1026$ kg m^{-3} is the Boussinesq reference density, $c_p = 3991.9$ J kg^{-1} k^{-1} is the specific heat capacity, L_x is the zonal extent of the ocean, $-H$ is the depth of the seabed, and η is the height of the free surface. The operators used are as follows: The symbol $\overline{\bullet}$ indicates a time average, $\bullet'$ indicates the deviation from the time average, $\langle \bullet \rangle$ indicates a zonal average, and $\bullet^*$ indicates deviations from the zonal mean.

The first two terms on the right-hand side of Eq. (1) are the Eulerian $\langle \overline{v_E} \rangle \langle \overline{T} \rangle$ and bolus $\langle \overline{v_B} \rangle \langle \overline{T} \rangle$ zonal-mean heat transport. They largely reflect the overturning and generally counteract one another (Fig. S7). The next two terms in Eq. (1) are the Eulerian $\langle \overline{v_E^* \, T^*} \rangle$ and bolus $\langle \overline{v_B^* \, T^*} \rangle$ heat transport from standing meanders; by construction, this includes any deviations from a strictly zonal flow. Figure S8 and Figs. 6d and 6i show that the Eulerian meridional standing eddy heat transport consists of contributions from the western boundary return flow and related standing meanders in the separation

of the gyres. Finally, the last term $\langle \overline{v'T'} \rangle$ in Eq. (1) is the total transient contribution. Thus, Fig. 14 allows us to attribute differences in total heat transport to these processes. Supporting information Figures S6–S9 show spatial plots of these same terms.

Negative numbers in the bottom-right inset in Fig. 14 indicate total heat crossing the shelf toward the ice front. The heat transport changes are consistent with the documented temperature changes at the ice front (Fig. 8). As a constant offset is added to the winds, Fig. 8 shows warming when comparing within each boundary condition and Fig. 14 corroborates this with the change in total advective heat transport. In more detail, for fully reentrant, Figs. 8b–e show increasingly warmer temperatures and the corresponding values in the inset in Fig. 14 show increasingly stronger total southward heat transport, similarly for the blocked shelf (Figs. 14f–j), blocked deep ocean (Figs. 14k–m colder than Figs. 14n,o), and full south–north block (Figs. 14p–t).

For heat transport across the shelf with a partially blocked western boundary (i.e., most simulations), Fig. 14 shows that the most important term in the advective heat balance is the Eulerian zonal-mean heat transport $\langle \overline{v_E} \rangle \langle \overline{T} \rangle$, particularly for simulations with control or positive offset winds (Figs. 14c–e,h–j,m–o). Since this term represents the Eulerian overturning circulation, it is unsurprising that the plan view plot of this term (Fig. S7) shows changes that are consistent with the changes in Ekman overturning cells discussed earlier (sections 2b and 4 earlier). In most of the remaining cases with an unblocked western boundary (Figs. 14a,b,k,l), under negative offset winds, the bolus term $\langle \overline{v_B} \rangle \langle \overline{T} \rangle$ becomes important. Interestingly, the top inset of Figs. 14b, 14f, 14g, and 14k–m shows that the leading term that transports heat toward the ice front can be different south and north of the shelf break. In the case of a fully blocked western boundary (bottom row in Fig. 14), north and south of the shelf break, the Eulerian $\langle \overline{v_E^*} \, \overline{T^*} \rangle$ heat transport from standing meanders is the most important term. Comparing the bottom row to cases with a reentrant boundary on the shelf, Fig. S8 (top) shows an increase in southward heat transport on the shelf by the Eulerian meridional standing eddy heat transport. In terms of the modest temperature changes in a fully blocked regime under a change in winds (bottom row in Fig. 8), the modest warming is due to large-scale increases in southward heat transport from $\langle \overline{v_E} \rangle \langle \overline{T} \rangle$ and localized shelf changes in $\langle \overline{v'T'} \rangle$ (bottom rows in Fig. 14, Fig. S7 top set, and Fig. S9).

5. Summary and discussion

In this study, we have explored how basin geometry and wind shifts have a large role in determining the temperature structure on Antarctica's shelf seas. Furthermore, the basin geometry influences how susceptible the shelf temperatures are to changes in winds.

We have used a simple barotropic model (Stommel's planetary geostrophic equations in section 2), to explore the linear dynamical balances that change when the circulation regime changes from a throughflow to a gyre, and we also examined how the Ekman and geostrophic circulations respond to

changes in surface forcing within these two regimes, all in the absence of baroclinicity and topography. We then used the primitive equation ocean model NEMO (section 4) with varying temperatures to see if the barotropic arguments from section 2 could offer a simplified interpretive framework, explaining some of the more complex circulation changes (section 4c). Despite the NEMO model configuration used here including complications such as bathymetry and baroclinicity, we find that the time-mean results are largely understood by the simple barotropic model. Fundamentally, the time-mean equilibrated differences between geometries and winds can be understood by changes in the Ekman layers and a geostrophic circulation compensating for changes in boundary conditions as a response to a fixed Ekman layer transport (sections 2a,b and 4c). Specifically, irrespective of boundary condition, the westerly and easterly stresses create a near-surface northward and southward transport in the top Ekman layer, respectively. As we discuss in sections 2 and 4, the interior responds to these transports where the boundary condition determines how the response is constrained. In brief, we summarize the response as follows. In the case of a throughflow, as the easterly–westerly wind transition moves south, so does the confluence region in the bottom layers and, critically, the upwelling region that brings warm waters onto the shelf (section 2b). We note that these results are consistent with more realistic simulations in the Amundsen Sea (Caillet et al. 2023; Haigh et al. 2023). In a gyre regime, when a wall is introduced, the return flow is no longer confined to the frictionally balanced bottom Ekman layers, but rather a wall creates topographic form stress enabling a geostrophic return flow at every depth where the wall is present. We noted that the introduction of a deep-ocean wall (Fig. 7) led to the flattening of isotherms in the deep ocean, with less warm waters close to the shelf. Applying the above arguments, we see this is because the return flow set up by the top Ekman transport is more evenly distributed throughout the water column than when the return flow is in the frictionally balanced bottom Ekman layer. While these largely linear dynamic balances have been understood for some time (e.g., Veronis 1996; Vallis 2017), we think this is the first time they have been revisited in terms of Antarctic shelf temperatures, with combinations of circulation regimes, in a realistic primitive equation ocean model.

When it comes to understanding future Southern Ocean projections, from the gyre regime simulations with a constant offset in the winds, we think this work demonstrates that we need to diagnose how the winds change, i.e., strength, a latitudinal shift, and a change in curl, as this will allow us to manage our expectations for the change we expect. Several studies have focused on eddies as a critical feature for fluxing heat and mass across the shelf break (Stern et al. 2015; Stewart and Thompson 2015; St-Laurent et al. 2013). In this instance, NEMO's momentum and heat budget show that over equilibrated time scales, the system response to surface forcing changes is explicable, to the first order, by linear dynamics. Some geometry changes, e.g., Figs. 7c and 7h and Figs. S3c and S3h, involve nonlinear advection, and some forcing perturbations involve eddies, e.g., Figs. 14a and 14b. The generally linear nature of the surface forcing response may be because of

the focus on equilibrated changes. Furthermore, while these simulations lack many important features (e.g., varying forcing, sea ice, ice shelves, meridional winds, and realistic bathymetry), we hope this study encourages others to consider basin geometry and easterlies in related idealized studies; our own work is ongoing in adding other features. One important undiscussed aspect is the buoyancy forcing (e.g., Hattermann 2018; Moorman et al. 2020). In the restoring approach used in this study, both the near-surface boundary stratification and the northern boundary stratification are being nudged toward a single state. As we have seen, varying the wind forcing leads to many final states; however, the use of restoring does mean there is an input of buoyancy at the boundaries that is different across each simulation. The importance of the buoyancy forcing is a topic of a follow-up study.

A remaining question is how the simplest of geometries and forcing considered here is relevant to the real ocean. To manage expectations, as winds change, we need metrics to diagnose when we are in a throughflow or gyre regime. Blocked f/h contours offer some barotropic insights here, but the mechanisms described in this paper apply in partial cases too. In this study, we intentionally made the transitions distinct, making the diagnostics simple (section 4d), but in the real Southern Ocean, the dynamics is more mixed. Indeed, Masich et al. (2015) found that 95% of the momentum input by the wind at ACC latitudes is balanced by topographic form stress. We thus need a stratification-dependent metric to diagnose the degree to which a region is in a throughflow or gyre regime. We think work such as Fig. 5 from Waldman and Giordani (2023) or Fig. 9 from Khatri et al. (2024) diagnosing the dominant vorticity balance in different regions is working in the right direction. We assume this kind of diagnostic would need to reconcile throughflow and gyre dynamics into a singular framework; considerable discussion has occurred on this topic (Hughes 2000, 2002; Hughes and Cuevas, 2001; Jackson et al. 2006; Olbers 1998; Olbers et al. 2004; Warren et al. 1996). On applying Sverdrup theory in the Southern Ocean, Hughes (2002) used Sverdrup-like theories from Stommel (1957) and Webb (1993) to estimate ACC transport; see LaCasce and Isachsen (2010) for a more general review of linear theories. For vorticity in gyres alone, direct buoyancy forcing aside, the dominant terms are still debated. For example, Hughes (2000) notes that the historical tendency to focus on gyres in boxes with straight walls (Munk 1950; Stommel 1948) has led to the view that the return flow in western boundary currents occurs due to friction and viscosity. In reality, coastlines are sloped, leading to inviscid western currents where, like the throughflow regime, the wind stress is balanced by topographic form stress, or in vorticity parlance bottom pressure "torques" balance the wind stress curl (e.g., Schoonover et al. 2017; Styles et al. 2022). Here, we are interested in heat transport across Antarctica's shelf break. If we think of this in terms of momentum transport across f/h contours, then the above theories highlight (for vorticity) that momentum transport across a sloping shelf break or bottom ridge requires an additional source of vorticity, and the kind of dissipation (e.g., Munk and Stommel) changes depending on the nature of the feature. If we are to understand how Antarctica's shelf temperatures will respond to a warming

climate, then further work is needed on how to apply these ideas across mixed flow regimes.

APPENDIX

Nondimensionalization of Stommel (1948) Planetary Geostrophic Equations

The nondimensionalized form is obtained by starting with the dimensional, steady, linear, and depth-integrated equations: $H(f\mathbf{k} \times \mathbf{u}) = -H[(1/\rho_0)\nabla p] - r\mathbf{u} + (\boldsymbol{\tau}_x/\rho_0)$ and $H(\nabla \cdot \mathbf{u}) = 0$. Variables are defined as in the main text; additionally, H is the seafloor depth and ρ_0 is a reference density. We define scales for our nondimensional variables $\mathbf{x} = (x, y, z) = (L\hat{x}, L\hat{y}, H\hat{z})$, $\mathbf{u} = U\hat{\mathbf{u}}$, $p = P\hat{p}$, and $\boldsymbol{\tau}_x = \tau_0\hat{\boldsymbol{\tau}}_x$. We treat r and f as our problem's key parameters and so do not initially nondimensionalize them; this approach allows us to group all the other variables together. Substitution of these definitions leads to $HU(f\mathbf{k} \times \hat{\mathbf{u}}) = -H[(1/\rho_0)P\hat{\nabla}\hat{p}] - rU\hat{\mathbf{u}} + (\tau_0/\rho_0)\hat{\boldsymbol{\tau}}_x$ and $HU(\nabla \cdot \hat{\mathbf{u}}) = 0$. Now, assuming a leading balance between pressure and the wind stress term, as per Veronis (1966), gives $P \sim \tau_0 L/H$. Following Bryan (1963), we assume Sverdrup balance will hold over much of the domain and take $U = \tau_0/(\rho_0\beta HL)$, where $\beta = \partial f/\partial y$. Substitution of these two relationships into our two latest equations, with some cancellation, gives $\hat{f}\mathbf{k} \times \hat{\mathbf{u}} = -\hat{\nabla}\hat{p} - \hat{r}\hat{\mathbf{u}} + \hat{\boldsymbol{\tau}}_x$ and $\nabla \cdot \hat{\mathbf{u}} = 0$, where $\hat{f} = f/(\beta L)$ is the nondimensional Coriolis frequency and $\hat{r} = r/(\beta HL)$ is the nondimensional bottom friction. For convenience, we drop the circumflex accent in the main discussion above.

REFERENCES

Abernathey, R., J. Marshall, and D. Ferreira, 2011: The dependence of Southern Ocean meridional overturning on wind stress. *J. Phys. Oceanogr.*, **41**, 2261–2278, https://doi.org/10.1175/JPO-D-11-023.1.

Allison, L. C., H. L. Johnson, and D. P. Marshall, 2011: Spin-up and adjustment of the Antarctic Circumpolar Current and global pycnocline. *J. Mar. Res.*, **69**, 167–189, https://doi.org/10.1357/002224011798765330.

Armitage, T. W. K., R. Kwok, A. F. Thompson, and G. Cunningham, 2018: Dynamic topography and sea level anomalies of the Southern Ocean: Variability and teleconnections. *J. Geophys. Res. Oceans*, **123**, 613–630, https://doi.org/10.1002/2017JC013534.

Barnier, B., and Coauthors, 2006: Impact of partial steps and momentum advection schemes in a global ocean circulation model at eddy-permitting resolution. *Ocean Dyn.*, **56**, 543–567, https://doi.org/10.1007/s10236-006-0082-1.

Boyer, T. P., and Coauthors, 2018: World Ocean Atlas 2018. NOAA National Centers for Environmental Information, accessed 4 April 2019, https://www.ncei.noaa.gov/access/metadata/landing-page/bin/iso?id=gov.noaa.nodc:NCEI-WOA18.

Bracegirdle, T. J., E. Shuckburgh, J.-P. Sallee, Z. Wang, A. J. S. Meijers, N. Bruneau, T. Phillips, and L. J. Wilcox, 2013: Assessment of surface winds over the Atlantic, Indian, and Pacific Ocean sectors of the Southern Ocean in CMIP5 models: Historical bias, forcing response, and state dependence. *J. Geophys. Res. Atmos.*, **118**, 547–562, https://doi.org/10.1002/jgrd.50153.

Bryan, K., 1963: A numerical investigation of a nonlinear model of a wind-driven ocean. *J. Atmos. Sci.*, **20**, 594–606, https://doi.org/10.1175/1520-0469(1963)020<0594:ANIOAN>2.0.CO;2.

Caillet, J., N. C. Jourdain, P. Mathiot, H. H. Hellmer, and J. Mouginot, 2023: Drivers and reversibility of abrupt ocean state transitions in the Amundsen Sea, Antarctica. *J. Geophys. Res. Oceans*, **128**, e2022JC018929, https://doi.org/10.1029/2022JC018929.

Constantinou, N. C., and A. M. Hogg, 2019: Eddy saturation of the Southern Ocean: A baroclinic versus barotropic perspective. *Geophys. Res. Lett.*, **46**, 12 202–12 212, https://doi.org/10.1029/2019GL084117.

Donohue, K. A., K. L. Tracey, D. R. Watts, M. P. Chidichimo, and T. K. Chereskin, 2016: Mean Antarctic Circumpolar Current transport measured in Drake Passage. *Geophys. Res. Lett.*, **43**, 11 760–11 767, https://doi.org/10.1002/2016GL070319.

Dotto, T. S., and Coauthors, 2018: Variability of the Ross Gyre, Southern Ocean: Drivers and responses revealed by satellite altimetry. *Geophys. Res. Lett.*, **45**, 6195–6204, https://doi.org/10.1029/2018GL078607.

Farneti, R., and Coauthors, 2015: An assessment of Antarctic Circumpolar Current and Southern Ocean meridional overturning circulation during 1958–2007 in a suite of interannual CORE-II simulations. *Ocean Modell.*, **93**, 84–120, https://doi.org/10.1016/j.ocemod.2015.07.009.

Gent, P. R., and J. C. Mcwilliams, 1990: Isopycnal mixing in ocean circulation models. *J. Phys. Oceanogr.*, **20**, 150–155, https://doi.org/10.1175/1520-0485(1990)020<0150:IMIOCM>2.0.CO;2.

——, J. Willebrand, T. J. McDougall, and J. C. McWilliams, 1995: Parameterizing eddy-induced tracer transports in ocean circulation models. *J. Phys. Oceanogr.*, **25**, 463–474, https://doi.org/10.1175/1520-0485(1995)025<0463:PEITTI>2.0.CO;2.

Gnanadesikan, A., and R. W. Hallberg, 2000: On the relationship of the Circumpolar Current to Southern Hemisphere winds in coarse-resolution ocean models. *J. Phys. Oceanogr.*, **30**, 2013–2034, https://doi.org/10.1175/1520-0485(2000)030<2013:OTROTC>2.0.CO;2.

Gómez-Valdivia, F., P. R. Holland, A. Siahaan, P. Dutrieux, and E. Young, 2023: Projected West Antarctic Ocean warming caused by an expansion of the Ross Gyre. *Geophys. Res. Lett.*, **50**, e2023GL102978, https://doi.org/10.1029/2023GL102978.

Goyal, R., A. Sen Gupta, M. Jucker, and M. H. England, 2021: Historical and Projected changes in the Southern Hemisphere surface westerlies. *Geophys. Res. Lett.*, **48**, e2020GL090849, https://doi.org/10.1029/2020GL090849.

Gray, A. R., and S. C. Riser, 2014: A global analysis of sverdrup balance using absolute geostrophic velocities from Argo. *J. Phys. Oceanogr.*, **44**, 1213–1229, https://doi.org/10.1175/JPO-D-12-0206.1.

Haigh, M., P. R. Holland, and A. Jenkins, 2023: The influence of bathymetry over heat transport onto the Amundsen Sea continental shelf. *J. Geophys. Res. Oceans*, **128**, e2022JC019460, https://doi.org/10.1029/2022JC019460.

Hattermann, T., 2018: Antarctic thermocline dynamics along a narrow shelf with easterly winds. *J. Phys. Oceanogr.*, **48**, 2419–2443, https://doi.org/10.1175/JPO-D-18-0064.1.

Hidaka, K., and M. Tsuchiya, 1953: On the Antarctic Circumpolar Current. *J. Mar. Res.*, **12**, 214–222, https://elischolar.library.yale.edu/journal_of_marine_research/794/.

Hogg, A. M., and B. Gayen, 2020: Ocean gyres driven by surface buoyancy forcing. *Geophys. Res. Lett.*, **47**, e2020GL088539, https://doi.org/10.1029/2020GL088539.

Hughes, C. W., 1997: Comments on "On the obscurantist physics of 'form drag' in theorizing about the Circumpolar Current." *J. Phys. Oceanogr.*, **27**, 209–210, https://doi.org/10.1175/1520-0485(1997)027<0209:COOTOP>2.0.CO;2.

——, 2000: A theoretical reason to expect inviscid western boundary currents in realistic oceans. *Ocean Modell.*, **2**, 73–83, https://doi.org/10.1016/S1463-5003(00)00011-1.

——, 2002: Sverdrup-like theories of the Antarctic Circumpolar Current. *J. Mar. Res.*, **60** (1), 1–17, https://doi.org/10.1357/002224002762341221.

——, and B. A. de Cuevas, 2001: Why western boundary currents in realistic oceans are inviscid: A link between form stress and bottom pressure torques. *J. Phys. Oceanogr.*, **31**, 2871–2885, https://doi.org/10.1175/1520-0485(2001)031<2871:WWBCIR>2.0.CO;2.

IOC, SCOR, and IAPSO, 2010: The international thermodynamic equation of seawater—2010: Calculation and use of thermodynamic properties. Intergovernmental Oceanographic Commission Manuals and Guides 56, 218 pp., http://www.teos-10.org/pubs/TEOS-10_Manual.pdf.

Jackson, L., C. W. Hughes, and R. G. Williams, 2006: Topographic control of basin and channel flows: The role of bottom pressure torques and friction. *J. Phys. Oceanogr.*, **36**, 1786–1805, https://doi.org/10.1175/JPO2936.1.

Karnauskas, K., 2020: *Physical Oceanography and Climate.* Cambridge University Press, 247 pp., https://doi.org/10.1017/9781108529594.

Khatri, H., S. M. Griffies, B. A. Storer, M. Buzzicotti, H. Aluie, M. Sonnewald, R. Dussin, and A. Shao, 2024: A scale-dependent analysis of the barotropic vorticity budget in a global ocean simulation. *J. Adv. Model. Earth Syst.*, **16**, e2023MS003813, https://doi.org/10.1029/2023MS003813.

LaCasce, J. H., and P. E. Isachsen, 2010: The linear models of the ACC. *Prog. Oceanogr.*, **84**, 139–157, https://doi.org/10.1016/j.pocean.2009.11.002.

Madec, G., and Coauthors, 2019: NEMO ocean engine, Zenodo, https://doi.org/10.5281/zenodo.3878122.

Masich, J., T. K. Chereskin, and M. R. Mazloff, 2015: Topographic form stress in the Southern Ocean state estimate. *J. Geophys. Res. Oceans*, **120**, 7919–7933, https://doi.org/10.1002/2015JC011143.

McWilliams, J. C., 2011: *Fundamentals of Geophysical Fluid Dynamics.* Cambridge University Press, 272 pp.

Meredith, M. P., and Coauthors, 2011: Sustained monitoring of the Southern Ocean at Drake Passage: Past achievements and future priorities. *Rev. Geophys.*, **49**, RG4005, https://doi.org/10.1029/2010RG000348.

Moorman, R., A. K. Morrison, and A. McC. Hogg, 2020: Thermal responses to Antarctic ice shelf melt in an eddy-rich global ocean–sea ice model. *J. Climate*, **33**, 6599–6620, https://doi.org/10.1175/JCLI-D-19-0846.1.

Morrison, A. K., A. M. Hogg, and M. L. Ward, 2011: Sensitivity of the Southern Ocean overturning circulation to surface buoyancy forcing. *Geophys. Res. Lett.*, **38**, L14602, https://doi.org/10.1029/2011GL048031.

——, W. G. C. Huneke, J. Neme, P. Spence, A. M. Hogg, M. H. England, and S. M. Griffies, 2023: Sensitivity of Antarctic shelf waters and abyssal overturning to local winds. *J. Climate*, **36**, 6465–6479, https://doi.org/10.1175/JCLI-D-22-0858.1.

Munday, D. R., H. L. Johnson, and D. P. Marshall, 2013: Eddy saturation of equilibrated circumpolar currents. *J. Phys. Oceanogr.*, **43**, 507–532, https://doi.org/10.1175/JPO-D-12-095.1.

——, ——, and ——, 2015: The role of ocean gateways in the dynamics and sensitivity to wind stress of the early Antarctic Circumpolar Current. *Paleoceanogr. Paleoclimatol.*, **30**, 284–302, https://doi.org/10.1002/2014PA002675.

——, X. Zhai, J. Harle, A. C. Coward, and A. J. G. Nurser, 2021: Relative vs. absolute wind stress in a circumpolar model of the Southern Ocean. *Ocean Modell.*, **168**, 101891, https://doi.org/10.1016/j.ocemod.2021.101891.

Munk, W. H., 1950: On the wind-driven ocean circulation. *J. Meteor.*, **7**, 80–93, https://doi.org/10.1175/1520-0469(1950)007<0080:OTWDOC>2.0.CO;2.

——, and E. Palmén, 1951: Note on the dynamics of the Antarctic Circumpolar Current. *Tellus*, **3**, 53–55, https://doi.org/10.1111/j.2153-3490.1951.tb00776.x.

Nadeau, L.-P., and R. Ferrari, 2015: The role of closed gyres in setting the zonal transport of the Antarctic Circumpolar Current. *J. Phys. Oceanogr.*, **45**, 1491–1509, https://doi.org/10.1175/JPO-D-14-0173.1.

Neme, J., M. H. England, and A. M. Hogg, 2021: Seasonal and interannual variability of the Weddell Gyre from a high-resolution global ocean-sea ice simulation during 1958–2018. *J. Geophys. Res. Oceans*, **126**, e2021JC017662, https://doi.org/10.1029/2021JC017662.

NOAA National Geophysical Data Center, 2009: ETOPO1 1 Arc-minute Global Relief Model. NOAA National Centers for Environmental Information, accessed 4 April 2019, https://www.ncei.noaa.gov/access/metadata/landing-page/bin/iso?id=gov.noaa.ngdc.mgg.dem:316.

Olbers, D., 1998: Comments on "On the obscurantist physics of 'form drag' in theorizing about the Circumpolar Current." *J. Phys. Oceanogr.*, **28**, 1647–1654, https://doi.org/10.1175/1520-0485(1998)028<1647:COOTOP>2.0.CO;2.

——, D. Borowski, C. Völker, and J.-O. Wölff, 2004: The dynamical balance, transport and circulation of the Antarctic Circumpolar Current. *Antart. Sci.*, **16**, 439–470, https://doi.org/10.1017/S0954102004002251.

——, K. Lettmann, and R. Timmermann, 2007: Six circumpolar currents—on the forcing of the Antarctic Circumpolar Current by wind and mixing. *Ocean Dyn.*, **57**, 12–31, https://doi.org/10.1007/s10236-006-0087-9.

——, J. Willebrand, and C. Eden, 2012: *Ocean Dynamics.* Springer, 703 pp., https://doi.org/10.1007/978-3-642-23450-7.

Park, Y.-H., and Coauthors, 2019: Observations of the Antarctic Circumpolar Current over the Udintsev Fracture Zone, the narrowest choke point in the Southern Ocean. *J. Geophys. Res. Oceans*, **124**, 4511–4528, https://doi.org/10.1029/2019JC015024.

Patmore, R. D., P. R. Holland, D. R. Munday, A. C. Naveira Garabato, D. P. Stevens, and M. P. Meredith, 2019: Topographic control of Southern Ocean gyres and the Antarctic Circumpolar Current: A barotropic perspective. *J. Phys. Oceanogr.*, **49**, 3221–3244, https://doi.org/10.1175/JPO-D-19-0083.1.

Pauthenet, E., J.-B. Sallée, S. Schmidtko, and D. Nerini, 2021: Seasonal variation of the Antarctic slope front occurrence and position estimated from an interpolated hydrographic climatology. *J. Phys. Oceanogr.*, **51**, 1539–1557, https://doi.org/10.1175/JPO-D-20-0186.1.

Pedlosky, J., 1996: *Ocean Circulation Theory.* Springer, 456 pp., https://doi.org/10.1007/978-3-662-03204-6.

Peña-Molino, B., M. S. McCartney, and S. R. Rintoul, 2016: Direct observations of the Antarctic Slope Current transport at 113°E. *J. Geophys. Res. Oceans*, **121**, 7390–7407, https://doi.org/10.1002/2015JC011594.

Petty, A. A., D. L. Feltham, and P. R. Holland, 2013: Impact of atmospheric forcing on Antarctic continental shelf water masses. *J. Phys. Oceanogr.*, **43**, 920–940, https://doi.org/10.1175/JPO-D-12-0172.1.

Pritchard, H. D., S. R. M. Ligtenberg, H. A. Fricker, D. G. Vaughan, M. R. van den Broeke, and L. Padman, 2012: Antarctic ice-sheet loss driven by basal melting of ice shelves. *Nature*, **484**, 502–505, https://doi.org/10.1038/nature10968.

Purich, A., and M. H. England, 2021: Historical and future projected warming of Antarctic shelf bottom water in CMIP6 models. *Geophys. Res. Lett.*, **48**, e2021GL092752, https://doi.org/10.1029/2021GL092752.

Schoonover, J., W. K. Dewar, N. Wienders, and B. Deremble, 2017: Local sensitivities of the Gulf Stream separation. *J. Phys. Oceanogr.*, **47**, 353–373, https://doi.org/10.1175/JPO-D-16-0195.1.

Spence, P., S. M. Griffies, M. H. England, A. M. Hogg, O. A. Saenko, and N. C. Jourdain, 2014: Rapid subsurface warming and circulation changes of Antarctic coastal waters by poleward shifting winds. *Geophys. Res. Lett.*, **41**, 4601–4610, https://doi.org/10.1002/2014GL060613.

——, R. M. Holmes, A. M. Hogg, S. M. Griffies, K. D. Stewart, and M. H. England, 2017: Localized rapid warming of West Antarctic subsurface waters by remote winds. *Nat. Climate Change*, **7**, 595–603, https://doi.org/10.1038/nclimate3335.

Stern, A., L.-P. Nadeau, and D. Holland, 2015: Instability and mixing of zonal jets along an idealized continental shelf break. *J. Phys. Oceanogr.*, **45**, 2315–2338. https://doi.org/10.1175/JPO-D-14-0213.1.

Stewart, A. L., 2021: Warming spins up the Southern Ocean. *Nat. Climate Change*, **11**, 1022–1024, https://doi.org/10.1038/s41558-021-01227-y.

——, and A. F. Thompson, 2012: Sensitivity of the ocean's deep overturning circulation to easterly Antarctic winds. *Geophys. Res. Lett.*, **39**, L18604, https://doi.org/10.1029/2012GL053099.

——, and ——, 2015: Eddy-mediated transport of warm circumpolar deep water across the Antarctic shelf break. *Geophys. Res. Lett.*, **42**, 432–440, https://doi.org/10.1002/2014GL062281.

——, J. C. McWilliams, and A. Solodoch, 2021: On the role of bottom pressure torques in wind-driven gyres. *J. Phys. Oceanogr.*, **51**, 1441–1464, https://doi.org/10.1175/JPO-D-20-0147.1.

St-Laurent, P., J. M. Klinck, and M. S. Dinniman, 2013: On the role of coastal troughs in the circulation of warm circumpolar deep water on Antarctic shelves. *J. Phys. Oceanogr.*, **43**, 51–64, https://doi.org/10.1175/JPO-D-11-0237.1.

Stommel, H., 1948: The westward intensification of wind-driven ocean currents. *Eos, Trans. Amer. Geophys. Union*, **29**, 202–206, https://doi.org/10.1029/TR029i002p00202.

——, 1957: A survey of ocean current theory. *Deep-Sea Res.*, **4**, 149–184, https://doi.org/10.1016/0146-6313(56)90048-X.

Straub, D. N., 1993: On the transport and angular momentum balance of channel models of the Antarctic Circumpolar Current. *J. Phys. Oceanogr.*, **23**, 776–782, https://doi.org/10.1175/1520-0485(1993)023<0776:OTTAAM>2.0.CO;2.

Styles, A. F., M. J. Bell, D. P. Marshall, and D. Storkey, 2022: Spurious forces can dominate the vorticity budget of ocean gyres on the C-grid. *J. Adv. Model. Earth Syst.*, **14**, e2021MS002884, https://doi.org/10.1029/2021MS002884.

Tansley, C. E., and D. P. Marshall, 2001: On the dynamics of wind-driven circumpolar currents. *J. Phys. Oceanogr.*, **31**, 3258–3273, https://doi.org/10.1175/1520-0485(2001)031<3258:OTDOWD>2.0.CO;2.

Thompson, A. F., A. L. Stewart, P. Spence, and K. J. Heywood, 2018: The Antarctic Slope Current in a changing climate. *Rev. Geophys.*, **56**, 741–770, https://doi.org/10.1029/2018RG000624.

Tsujino, H., and Coauthors, 2018: JRA-55 based surface dataset for driving ocean–sea-ice models (JRA55-do). *Ocean Modell.*, **130**, 79–139, https://doi.org/10.1016/j.ocemod.2018.07.002.

Vallis, G. K., 2017: *Atmospheric and Oceanic Fluid Dynamics: Fundamentals and Large-Scale Circulation.* 2nd ed. Cambridge University Press, 936 pp., https://doi.org/10.1017/9781107588417.

Verfaillie, D., and Coauthors, 2022: The circum-Antarctic ice-shelves respond to a more positive Southern Annular Mode with regionally varied melting. *Commun. Earth Environ.*, **3**, 139, https://doi.org/10.1038/s43247-022-00458-x.

Veronis, G., 1996: Effect of a constant, zonal wind on wind-driven ocean circulation. *J. Phys. Oceanogr.*, **26**, 2525–2528, https://doi.org/10.1175/1520-0485(1996)026<2525:EOACZW>2.0.CO;2.

Visbeck, M., J. Marshall, T. Haine, and M. Spall, 1997: Specification of eddy transfer coefficients in coarse-resolution ocean circulation models. *J. Phys. Oceanogr.*, **27**, 381–402, https://doi.org/10.1175/1520-0485(1997)027<0381:SOETCI>2.0.CO;2.

Waldman, R., and H. Giordani, 2023: Ocean barotropic vorticity balances: Theory and application to numerical models. *J. Adv. Model. Earth Syst.*, **15**, e2022MS003276, https://doi.org/10.1029/2022MS003276.

Warren, B. A., J. H. LaCasce, and P. E. Robbins, 1996: On the obscurantist physics of "form drag" in theorizing about the Circumpolar Current. *J. Phys. Oceanogr.*, **26**, 2297–2301, https://doi.org/10.1175/1520-0485(1996)026<2297:OTOPOD>2.0.CO;2.

Webb, D. J., 1993: A simple model of the effect of the Kerguelen Plateau on the strength of the Antarctic Circumpolar Current. *Geophys. Astrophys. Fluid Dyn.*, **70**, 57–84, https://doi.org/10.1080/03091929308203587.

——, R. M. Holmes, P. Spence, and M. H. England, 2019: Barotropic Kelvin wave-induced bottom boundary layer warming along the West Antarctic Peninsula. *J. Geophys. Res. Oceans*, **124**, 1595–1615, https://doi.org/10.1029/2018JC014227.

Whitworth, T., III, A. H. Orsi, S.-J. Kim, W. D. Nowlin Jr., and R. A. Locarnini, 1998: Water masses and mixing near the Antarctic slope front. *Ocean, Ice, and Atmosphere: Interactions at the Antarctic Continental Margin*, S. S. Jacobs and R. F. Weiss, Eds., Antarctic Research Series, Vol. 75, American Geophysical Union, 1–27.

Wilson, E. A., A. F. Thompson, A. L. Stewart, and S. Sun, 2022: Bathymetric control of subpolar gyres and the overturning circulation in the Southern Ocean. *J. Phys. Oceanogr.*, **52**, 205–223, https://doi.org/10.1175/JPO-D-21-0136.1.

Zhai, X., and D. R. Munday, 2014: Sensitivity of Southern Ocean overturning to wind stress changes: Role of surface restoring time scales. *Ocean Modell.*, **84**, 12–25, https://doi.org/10.1016/j.ocemod.2014.09.004.